University of Bremen

Institute of Environmental Physics (IUP)

Remote Sensing of Polar Regions

Master thesis

Sea Ice Drift and Deformation from SAR Satellite Data in the Area of the MOSAiC Expedition

Hamoun Heidari Bateni

3121355 – 06.09.81

First Supervisor:

Dr. Gunnar Spreen

Second Supervisor:

Prof. Dr. Wolfgang Dierking

25 September 2020

Abstract

Sea ice deforms continually due to the forcing of winds and ocean currents. Ultimately the ice cover of the Arctic Ocean breaks into an aggregation of ice floes. Strips of open water, so-called leads, and pressure ridges consisting of ice fragments that were piled up due to compressive forces are found along the floe edges. These ice surface features have an intense on the interaction of sea ice with the atmosphere and their corresponding bottom features with the ocean, as they alter heat and gas fluxes regulation, brine rejection, sea ice mass balance, and air and water drag.

The goal of this thesis is to provide and investigate sea ice deformation in the vicinity of the German research vessel Polarstern while it was drifting through the Arctic during the MOSAiC expedition. Sea ice drift and deformation are quantified by using a pair of Sentinel-1 SAR data. At first, sea ice drift is retrieved and then deformation parameters such as divergence and shear will be calculated from the drift data. To test how well-behaved and practical the sea ice deformation retrieval is, the following research questions are addressed: (1) how well the algorithm is suited to derive deformation? and (2) can handle real deformation events and is a sea ice deformation event associated with a meteorological event?

The algorithm consists of two steps. In the first step, an open-source drift retrieval algorithm from NERSC, Norway is exploited (Korosov and Rampal, 2017). It consists of two major phases: i) utilizing a feature tracking approach to have a first assessment of sea ice motion and ii) applying a correlation-based pattern matching technique to spot corresponding sea ice structures in a sequence of images (the algorithm written by Korosov and Rampal, 2017, is available in GitHub).

In the second stage, based on Lindsay and Stern (2003), a sea ice deformation retrieval algorithm is developed and implemented by the author to calculate deformation parameters such as divergence and shear by exploiting the vector field of drift from the first step and then evaluate the algorithm during a sea ice opening event to answer the first question.

In conclusion, the algorithm is used to provide time-series of mean values of deformation parameters in three different area sizes around ice breaker Polarstern during the MOSAiC expedition and observe deformation events and afterward, the result will be compared with meteorological data from the Polarstern to answer the second question. In future work, this method could be implemented for other satellites like TerraSAR-X to fill gaps of time-series due to the lack of Arctic pole coverage of Sentinel-1 and also the result could be evaluated with in-situ deformation data from MOSAiC expectation (such as buoy data from Polarstern).

Contents

1 | Introduction

The phrase “sea ice” is used to nominate all types of ice coming from freezing ocean and sea water. Sea ice formation starts with frazil ice formation. During this process, a large amount of salt is discharged into the beneath ocean water, while some remains trapped in the sea ice as brine pockets. Those pockets are being evacuated over time by a drainage/percolation process of the brines through the sea ice, allowing the ice cover to become much the same to fresh ice within a couple of months. Ice growth pursues over processes such as pancake formation, rafting, ridging, and consolidation, the occurrence of which depends on atmospheric and ocean conditions (calm or agitated). Eventually, this sometimes leads to the formation of a practically continuous sheet of ice a few meters thick that floats on top of the ocean, stretching over thousands of kilometers; this is frequently named the “sea ice pack” or “sea ice cover.” A sea ice pack should not be confused with the ice sheets or ice shelves made from freshwater ice formed by a slow compaction process of snow and typically from hundreds to thousands of meters thick (Carrieres et al., 2017). Sea ice drifts on the ocean surface mainly due to wind stress and ocean currents. The spatial disagreement of these forces generates internal sea ice stress gradients that induces deformation of sea ice (Spreen et al., 2017). It is essential to have reliable information of sea ice deformation and its movement whereas it affects the climate system, human life (e.g. as a place for activities like hunting), natural environment (e.g. ecological habitat) and industry in the polar regions (e.g. a barrier for naval transportation such as the Northwest or the Northeast Passage, and offshore structures as lighthouses or oil platforms).

The history of scientific measurements of sea ice drift goes back to more than a century ago when Fridtjof Nansen moored his ship (Fram) to the sea ice and drifted with it over the Eurasian Arctic Ocean at the time of his expedition from 1895 to 1898. He reported that the direction of wind-induced sea ice drift has a 30 ° deviation to the right side of the wind vector with a speed which is roughly 2 % of the wind speed (Nansen, 1902). For the next decades, many successful researches have been organized on sea ice kinematics using buoys, drift stations and ship observations. In the meantime, however the measurements and subsequent sea ice information were obtained with high temporal resolution, they were spatially sporadic. The poor spatial resolution, was a barrier in the scientific research on the Arctic-wide motion of sea ice and therefore, subsequent estimated deformation. At late 1970’s , satellite data put an end to this constrain and made it possible to retrieve the motion of sea ice at high spatial resolutions utilizing a sequence of satellite images (Fily and Rothrock, 1986) and even later for sea ice deformation (Fily and Rothrock, 1990).

Seasat was the pioneer satellite formed for remote sensing of the Earth's oceans and had on board the first space-borne Synthetic Aperture Radar (SAR). It was launched on 27 June 1978. Hall and Rothrock (1981) retrieved sea ice drift manually. In 1987, Fily and Rothrock presented the first non-manual sea ice drift algorithms based on pattern-matching (cross-correlation) employing a resolution pyramid to boost computational loads. To avoid resolution pyramid, Collins and Emery (1988) computed the correlation in the Fourier domain. Fily and Rothrock (1990) was pioneer in detecting opening and closing by using classification on SAR satellite images. Kwok et al. (1990) developed the first operational sea ice drift retrieval system, called Geophysical Processing System (GPS) at the Alaska SAR Facility based on ERS-1 data. Lindsay and stern (2003) calculating deformation parameters by computing partial derivatives of vector field of drift. In 2008, Thomas et al. developed an algorithm form on pattern-matching that involved the two phase-correlation and cross-correlation on ERS-1 SAR images (spatial resolution: up to 400 m). This algorithm has been recommenced by Holland and Dierking (2011), but on ENVISAT ASAR images. Subsequently, Muckenhuber et al. (2016) developed an open-source feature-tracking algorithm based on corner detection technique named ORB (More details are made clear in section 2) on Sentinel-1 SAR images which was pusued by Korosov and Rampal (2017). The algorithm (based on Korosov and Rampal (2017)) is available in the GitHub and it is used as step in this study (https://github.com/nansencenter/sea_ice_drift).

1.1 Significance of sea ice

Sea ice plays a pivotal role in the climate system. It seperates the relatively warm ocean water from the severely cold air (especially in winter) and thereupon leads to a decrease in the solar radiation absorption by the ocean water. The sea ice existence boosts the albedo of the ocean surface and therefore the extent, thickness, and concentration of sea ice and have a direct effect on the heat exchange between the atmosphere and ocean (Vaughan et al., 2013). Sea ice formation induces the latent heat to be surrendered to the ocean. Besides, salt cannot be part of sea ice crystal and the formation of ice crystal rejects salts into the ocean underneath, but the salinity of young ice is still significance. As it becomes older (usually means thicker), its salinity drops (due to phenomena such as brine rejection). So the introductory phenomenon diminish the stratification of ocean water. Vice versa, the ocean surface layer evolves into a fresher and more stable situation, when the ice melts (Yang and Neelin, 1993) (Mean salinity of multi-year ice is between 2% and 3% depending on season (Cox and Weeks, 1974))

The reality that sea ice is a cluster of foes adjusts its interaction with other climate elements, like the ocean and the atmosphere. For the time being of winter, sea ice plays as an insulator (as mention before). By that, sea ice and particularly its snow cover more and more lessen the growth rate of ice as it gets thicker. In a lead, the ocean is in immediate connection with the air, so that intense heat loss is initiated and thereupon young ice is formed. The relatively dark ocean water in a lead absorbs more short-wave radiation than shinny ice generated by the lower albedo of open ocean. A comparably warmer ocean and the lateral melting adjacent the foe edges stimulates the erosion of the ice foes in summer (Horvat et al., 2016). This feedback stimulates the retreat of the ice boundary during the swell of Arctic storms is fracturing the ice (Asplin et al., 2012). Additionally, short-wave radiation going through the ocean is a point of supply of energy for primary production (Nomura et al., 2018). Moreover, pressure ridges have also an impact on Arctic climate system: (1) pressure ridges rise the interfaces (with atmosphere and ocean) roughness of sea ice, which eventually changes the form drag (Arya, 1973; Tsamados et al., 2014), (2) snowdrifts form nearby pressure ridges (Iacozza & Barber, 1999), and (3) the keels of pressure ridges are landed in not deep places of the Arctic Basin, so that stable and static ice ahead the shore, so-called fast-ice (or land fast-ice), is formed (Mahoney et al., 2007; Lemieux et al., 2015).

The role of sea ice changes in the framework of global warming. The surface temperature in Arctic areas grows two times faster than the global mean, which is pointed out as Arctic amplification. Higher temperatures have produced a rapid fall in the Arctic sea ice extent over the past decades. In the time from 1979 to 2012 the minimum sea ice extent in September declined by more than 30 % (Stroeve et al., 2012) and the sea ice volume decreases by unexpectedly 70-80 % (Overland & Wang, 2013). The thinning follows in weaker ice that is more sensitive to deformation. Actually, the average drift of sea ice is stimulated by 17 % in winter and 8.5 % in summer, in combination with an escalation in deformation rates of 50 % between 1979 and 2007 (Rampal et al., 2009). Spreen et al., 2011 analyse the spatial trends in Arctic sea ice drift speed from satellite data and found the spatially mean trend in drift speed inside the Arctic Basin is 10.6% ± 0.9%/decade, and fluctuates between −4% and 16%/decade relying upon on the region. The raised breaking of the ice cover prompts a additional retreat of the ice cover because raised absorption of short-wave radiation and lateral melting enhance the melting of the sea ice. The Arctic Ocean is anticipated to become ice-free during summer within the first half of the 21st century (Overland & Wang, 2013).

The opening of the Arctic Ocean is “not just the best opportunity of our generation, but of the last 12,000 years” says Scott Minerd (The Sydney Morning Herald, May 3rd 2014, https://www.smh.com.au/business/arctic-investment-the-best-opportunity-of-last-12000-years-140502-37lv2.html [Status: 15.07.2020]), the chief investment officer of a large global investment and advisory firm (Guggenheim Partners LLC, https://www.guggenheimpartners.com [Status: 15.07.2020]). He referred to the growing economic attraction in the Arctic began by the decline of sea ice existence like: (1) shipping transport over the North Sea Route or the Northwest passage will be doable under climate change circumstances (Smith & Stephenson, 2013) and Arctic shipping rises already today (Eguıluz et al., 2016). (2) reasonable amounts of the wordwide oil and gas resources bury beneath the Arctic Ocean (Bird et al., 2008). (3) Arctic tourism is expanding (Hall & Saarinen, 2010; Maher, 2017). These economic movements and the Arctic climate change have a huge influence on native communities and the Arctic environment and creatures.

Interaction between the ice and atmospheric boundary layer and ocean surface layer leads to sea ice to drift and deform. For understanding of the atmosphere-ocean interface, it is crucial to examine the ice drift and deformation arrangement. Distict forces have a critical role in sea ice drift which are argued in the following section 1.2. Sea ice drift reorganize the sea ice from ice growth areas to ice fragmentation regions (e.g. transpolar drift). Sea ice motion can induce leads formation (through divergence) and ice deformed zones such as ridges and rubble fields (by virtue of convergence). In the shoreline area, under seaward wind sea ice drift (such as Katabatic wind) can produce large openings with a size between 10 km^2 to 100 000 km^2 named (coastal) polynya (Coastal polynya is only one kind of polynya). They play a crucial role in atmosphere and ocean exchange and makes an increased heat loss of the ocean and warming of the air column over (Lüpkes et al., 2008)

The motion of sea ice agrees to a negative transport of latent heat and fresh water because the phenomena which described before When sea ice melts at distinctive places because of drift, the water becomes cooler and gets fresher. In contrary, before drift, in areas of sea ice forming, ocean water gets warmer and saltier. This developes salinity and temperature gradients which can be a trigger to form movement between ice forming area and ice melting area. However, the melting of sea ice can enhance the stratification and slow down the polar deep convection as well (Leppäranta, 2011).

The transportation of sea ice from the Arctic Ocean through the Fram Strait into the Greenland sea is a fine case of huge amounts of drifting ice. The Fram Strait is acknowledged as the major path for

movement of ice departing the central Arctic ocean. In comparison, its outflow is approximately the equal volume as the river run-off from the surrounding landmasses (Siberia, Scandinavia, Canda and Alaska) into the Arctic ocean. The ice export through the Fram strait integrates to about 3×10^3 km^3 per year and alters the circulation of the Atlantic ocean and particularly the Gulf Stream (Hader, 1996; Leppäranta, 2011).

1.2 Sea ice drift

Sea-ice flows because of three significant forces: i) Wind stress; ii) Ocean currents; iii) Internal resistance (stress) of sea ice and two minor ones: i) Coriolis force and ii) Sea surface-tilt. The brief explanation of the 3 major factors comes as follow.

1.2.1 Wind stress

Wind forcing forces sea ice move by transferring momentum to the sea ice and also by determining the ocean surface currents. The rougher the surface of ice floe, the faster sea floe moves due to the winds contribution (increase in roughness boost ice drift that can cause more surface deformation formation which alter surface roughness again). Here is two example of wind-induced ocean surface current: the Beaufort Sea Gyre (BSG) and the Transpolar Drift Stream (TDS) (Thorndike and Colony, 1982; Leppäranta, 2011; Spreen et al., 2011).

1.2.2 Ocean currents

There are 3 types of current that have a augmentation to ice motion are: i) Permanent currents (such as East Greenland current); ii) periodic currents (tides), and iii) temporary currents (like local wind-induced currents). Ocean currents exert shear stress on ice. These stresses dominate sea ice motion in the long term scale (in the scale of month or year). This fact in most cases is valid, but in some certain areas, ocean currents can have short-term effects (e.g., short-term impact in sea ice modeling frequently means 1 hour to 10 days (Leppäranta, 2011)) (Shokr and Sinha., 2009; Kwok et al., 2013) (Fig 1.1).

1.2.3 Internal resistance (stress) of sea ice

The compactness and the strength of ice cover are two componants that generate the sea ice internal shear force and stress. In this case, the sea ice concentration (means surface fraction of ice in a region)

and mechanical stress are directly proportional contributors. Which the mechanical force depends on ice thickness, temperature, density, and porosity perform an decisive role in developing mechanical stress. Internal stress resistance among all 5 contributors in ice drift is the most variable one. Because for example, in a specific area, it affects the motion of small floes more than it affects big floes or in the same conditions for other forcing increase in ice concentration from a value between 0.4 and 0.6 to a high concentration (between 0.9 and 1.0) can reduce ice speed three times (Shokr and Sinha., 2009).

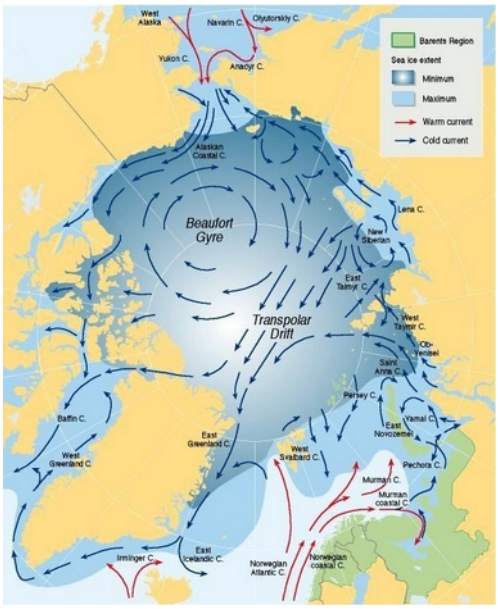

Fig 1.1 Arctic Ocean surface circulation. Red arrows indicate warm Atlantic Ocean currents and blue arrows indicate cold Arctic surface currents. North Atlantic drift waters entering the Arctic west of Svalbard flow counterclockwise at depth (the warm core is at roughly 300 meters) and exit through the Fram Strait. (Tremblay et al., 2007)

1.3 Sea ice drift observation and modeling

ice drift data can be measured with a high temporal resolution exploiting ground-based measurements such as drift buoys. Albeit, buoys are limited to a single measurements (which means its trajectory from installment to sinking time due to ice floe melting). It is not applicable for the entire area or basin specially if ice kinematics for an Eulerian reference system are needed (for example, matching a data position to the grid is difficult). For that reason, it is essential to find other methods for measurement of drift. Sea ice drift modeling is one solution for our issue. Drift retrieval from remote sensing data is another solution which is discussed in the following sections of this thesis. Sea ice models are

established on the dependency of drift on the wind stress, ocean currents, and the ice internal resistance with each other. Regardless of considerable usage of models, we also want satellite remote sensing to retrieve ice drift. In the satellite remote sensing, average displacement is retrieved by comparing sea ice pattern in two snapshots of a scene. The resulting drift fields from satellite observation is usually more similar to modeling than buoys observations. Because buoys follow ice floe (Lagrangian reference system), meantime, both modeling (To be precise it is the case for the most modeling approach not all. For example, some models use the Lagrangian approach, e.g. neXtSIM from Nansen Center, Rampal et al. (2016) or using RGPS (Lindsay and Stern, 2003)) and satellite observation measure sea ice drift as Eulerian reference system.

Altogether, modeling and satellite retrieval complete each other (e.g., satellite sea ice retrieval can be improved by means modeling because they can predict drift position which is helpful in satellite image selection (Kwok et al., 1990)). Modeled ice drift can be validated by both remote sensing observation and in-situ instruments. For example, Geiger et al., (1998) validate their model exploiting buoy observation. McLaren et al., (2006) evaluated the efficiency of their model by both buoy and satellite data.

Space-borne VNIR sensor (The visible and near-infrared fraction of the electromagnetic spectrum has wavelengths generally between 400 and 1100 nanometers (nm) (could be extended up to 2500 nm)) and SAR satellite data both provide high-resolution information. The benefits of VNIR sensors are: 1) fine spatial coverage and resolution; 2) Demanding less energy for image acquisition (as passive sensor); 3) easy to understand and interpret by producing RGB images. Concerning these advantages, VNIR remote sensing is an noteworthy tool for accessing the ice position during favorable conditions (e.g. cloud-free) and for validating other satellite sensors.

Nonetheless, VNIR sensors have a significant drawback in the polar regions. The disadvantage is being dependent on solar radiation and clear sky (cloud-free) situation that may induce having unreliable and erroneous data and noncontinuous year round monitoring. Therefore, our main source for uninterrupted sea ice screening with high temporal and spatial resolution is SAR data which is independent of the above-mentioned conditions. VNIR imagery are mainly used for interpretation support of the SAR scenes. Although VNIR in RGB format is easier to interpret, SAR images can reveal more detail than RGB images by understanding the sensor concept and the interaction of the electromagnetic waves with the sea ice surface.

In addition to sea ice motion and deformation as the topic of this work, SAR data can be used to provide information on ice/water classification and ice type classification as well. There are also other sea ice parameters like sea ice thickness, age and strength are retrieved using high-resolution sensors.

1.3.1 State of the art algorithms for detecting sea ice drift using SAR data

It is possible to retrieve ice drift manually or by using an automatic algorithm. Manual pattern recognition by human inspection is used to track sea ice motion with a fine accuracy but needs comparability large effort. In practice, high-resolution sea ice drift map generally are provided by an automatic retrieval algorithm and the manual approach solely used for validation purpose. In the both methods, it is necessary to utilize at least two consecutive images to follow sea ice formation and changes from one point in time and space to another (and have displacement as ouput).

Technically, SAR Doppler shift data can enable our analysis to retrieve instantaneous range velocity (which derive from one image) and it is a actual favored position because for example, in the Marginal Ice Zone (MIZ), due to low concentration of sea ice and its high degree of speed. We may have a large gap area in correlation approach result due to decorrelation which is not the case in Doppler examination or Doppler analyses gave us the traveled distance (the complex trajectory) not a straight distance (displacement). But this type of retrieval are in early level and there are also obstacles in exploiting them on Sentinel-1 Doppler data and they have disadvantage as followed:

i) suitable calibration of the SAR Doppler shifts are very demanding (Hansen et al., 2010; Kremer et al., 2017)

ii) only the line-of-sight motion can detectable (Hansen et al., 2010; Kremer et al., 2017).

iii) for typical ice speeds, the uncertainties quickly grow beyond the speed that we are trying to measure (kremer et al., 2017).

therefore it is expelled from this study.

There are various methods for tracking of displacements between two images. Among all, these four are the most routine ones in sea ice remote sensing:

i) optical flow / gradient-based motion tracking methods (Sun, 1996);

ii) pattern matching (Fily and Rothrock, 1987, Kwok et al., 1990 and 1998; Drinkwater, 1998; Karvonen, 2012; Komarov and Barber, 2014; Korosov and Rampal, 2017; Muckenhuber and Sandven, 2017);

iii) feature tracking methods (Daida et al., 1990; McConnell et al., 1991; Giles et al., 2011; Muckenhuber et al., 2016);

iv) wavelet analysis (Liu et al., 1997)

v) Doppler analyses (Hansen et al., 2010; kremer et al., 2017)

There are other approaches which combine the benefits of second and third methods (Vesecky et al., 1988; Kwok et al., 1990; Berg and Eriksson 2014) The algorithm used in this study be affiliated with this category.

1.4 Sea ice deformation

The North Pole has been one of the last unvisited locations on Earth that cast its spell on human beings. The North Pole lies in a sea — the Arctic Ocean. The outer layer of the Arctic Ocean is iced because of the low temperatures, forming a layer of ice. Around the beginning of the 20th century fearless adventurers with daring ideas directed North, and were challenged by the severe environment and the harsh weather conditions. Fridtjof Nansen and his associate Hjalmar Johansen had traveled with their ship "Fram" 18 month with the ice (Nansen, 1902), before they left it behind in March 1895 to commence their march to the pole. The first few days they could ski on heavy ice, nevertheless as they extended into the ice, skiing status became harder and harder. After 25 days of journey, Nansen and Johansen were confronting completely deformed ice that Nansen explained in the citation above on the evening before they needed to turn back. The ice was piled up in interminable ridges such powerfully as a results of ice deformation that a flow more North was impractical.

Oriented fractures distribute Arctic sea ice throughout a year. They disperse the ice cover into abundant ice foes and narrow bands of open water (Marko & Thomson, 1977; Kwok, 2001; Richter-Menge et al., 2002). The disintegration of ice is generated by stress developing from surface wind associated with weather orders, ocean eddies, geometric borderlines like the shoreline or a land-fast ice outline (Richter-Menge et al., 2002), tides (Holloway & Proshutinsky, 2007), ocean waves (Squire et al., 1995), or swell originating from Arctic strong weathers (Asplin et al., 2012). Convergent movement in the ice pack shapes pressure ridges whereas bands of open ocean, so-called leads, establish during divergent movement. These slender and lengthy forms are often referred to as Linear Kinematic Features (LKF) because of their establishment by the kinematic processes: opening, closing, and shear (Kwok, 2001).

The pack ice in the Arctic Ocean is nearly regularly in a movement because of the forcing by the wind stresses and ocean currents. The field of movement has a rather sophisticated form,since the existence of shoreline and horizontal gradients in the forcing give increase to convergent, divergent, and shearing motions on a broad extent of horizontal scales. Such movements generate ice deformation and are the explanation for the observed large fluctuations of the ice thickness even on very small scales.

Convergent movements lead to in rafted and ridged forms over a wide thickness interval, from a few centimeters to several tens of meters, based on, among various factors, the thickness of the ridging ice. Thin ice shapes very quickly during the winter,in freshly opened leads in the divergent areas, and then grows over the seasons to intermediate thicknesses, so called first-year ice (First-Year Ice (FYI) is ice that grows in the polar winter (after it has gone over the new ice – nilas – young ice phases and grows further) but does not survive the polar summer months (it melts away)). Ultimately, while the floes are very old, they may reach an equilibrium thickness when the accretion during the winter equals the ablation during the summer so they can survive at least on polar summer then they called Multi-Year Ice (MYI).

The divergence (The difference, opening minus closing, is the net fractional area change or divergence of the scene.) procedure generates ice in the thickness extent from close to zero and up to about 3-4 m, which is the equilibrium thickness in the Arctic Ocean. Large-scale shearing movements in association with cracks and leads might produce convergence and divergence regionally and in this manner force both new ice production and ridge formation [Thordike et al., 1975].

Arctic sea ice is altering, it is getting thinner (Kwok & Cunningham, 2015), more dynamic (Spreen et al., 2011), and simultaneously the deformation processes are flourishing (Itkin et al., 2017; Rampal et al., 2009). These alteration should induce a surge in the contribution of deformed sea ice in the dispersion of first year sea ice thickness

Itkin and colleagues in 2017 had a case study that over the survey their region they estimated that around 1.3% of level sea ice volume was compressed jointly into deformed ice and the new ice produced in leads in 7 days following the deformation event would build up the sea ice volume by 0.5%

Sea ice the most part of time deforms and reorganized at the time of a temporally individual atmospheric induced events like storms and unexpected wind direction alterations (Hutchings et al., 2011; Itkin et al., 2017)

The opening (freshly opened leads are a origin of new ice production, brine rejection to the ocean water, and very quick heat transfer from the relatively warm ocean to the very cold atmosphere. These regions govern the regional heat flux into the atmosphere and brine flux into the mixed layer (Kwok 2006).) /closing (Closings of the ice cover induces ice to raft and to pile up into pressure ridges and pushed down into keels boosting the ice-atmosphere and ice-ocean drag (Kwok 2006).) of open water regions taking place over most deformation strips have a large influence on the regional and Arctic-wide sea ice and ocean states, as it impacts the ice growth and ice mass balance, the ocean-atmosphere vertical heat fluxes, and the upper ocean salinity by brine rejection [Kwok et al., 2008; McPhee et al., 2005; Aagaard et al., 1981; Nguyen et al., 2012].

The brine rejection (salt rejection) from new ice (e.g. in leads) contributes in maintaining of the Arctic ocean halocline (a cline is a comparatively thin, typically horizontal layer within a fluid, in which a property of the fluid varies greatly over a relatively short vertical distance, so halocline is a horizontal layer of ocean with a strong, vertical salinity gradient) and also governs secondary circulation arrangement in the upper ocean (Morison et al. 1992).

Literally, the long tail of the ice thickness arrangements is generally the consequence of the mechanical alteration of the thinner, undeformed ice in the leads into the thicker, deformed ice of the ridges. The ridging procedure is not only a deformational energy sink but in some areas ridges account for 20 per cent or more of the total ice volume (Koerner 1973).

Rising deformation indicates more powerful fracturing, for that reason more lead opening, and therefore a declining albedo. This accelerates sea ice thinning in summer and hinders refreezing in early winter, therefore declining the mechanical strength of the cover and granting even more fracturing, greater drifting speed and deformation, and probably a quicker transport of sea ice over the Fram Strait. These rises in both sea ice mean speed and deformation rate are improbable to be a outcome of a more powerful atmospheric forcing, suggesting alternatively that sea ice kinematics act a major role in the albedo feedback loop and sea ice decline (Rampal et al., 2009).

As deformation resolves sea ice opening (i.e., positive divergence) and closing (i.e., negative divergence), it may be employed to assess significant global quantities, like the ice growth in leads, with some presumptions on sea ice production and redistribution (Kwok et al., 1995). Exploiting the RGPS data set, Kwok (2006) determined that deformation related ice growth is about 25–40 % of the winter ice growth in both the perennial and seasonal ice regions. Kwok et al. (2008) also illustrated that the deformation-related ice growth acquired from the RGPS data set is up to 2 times higher than the

one determined by numerical models, indicating a possible underestimate of the associated sea ice–ocean feedbacks (Bouillon and Rampal, 2015).

In addition to vital facts about sea ice opening and closing, the interpretation of sea ice movement and deformation additionally delivers a special understanding into the fundamental physics regulating the sea ice dynamics and brings precious information with which to validate sea ice models Marsan et al. (2004) expressed how the statistics of sea ice deformation alter as a function of spatial scale, at the same time Rampal et al. (2008) generalized these scaling characteristics to both the spatial and temporal domains. Stern and Lindsay (2009) and Herman and Glowacki (2012) cited the seasonal and interannual variability of the spatial scaling exponents. Girard et al.(2009, 2011) illustrated that classical sea ice models do not catch these statistical characteristics.

Sea ice motion can generate different type of surface deformation features, where it can be classified in two groups: (i) fractures and (ii) rafting and pressure ridging.

1.4.1 Fractures

The word “fracture” directs to any opening that reveals seawater to the atmosphere. It may take the form a crack or a lead (definitions are furnished in “Manual of Standard Procedures for Observing and Reporting Ice Conditions” [MANICE, 2005]). Fracture also defines as “any break or rupture through very close ice, compact ice, consolidated ice, fast ice, or a single floe resulting from deformation processes. Fractures may contain brash ice and/or be covered with nilas and/or young ice. Length may vary from a few meters to many kilometers” [Sea ice Nomenclature March 2014].

1.4.1.1 Cracks

Cracks are the opening in an ice sheet, which are evolved while the sheet diverges or shears in order to ease the localized tensile stresses [Schulson and Hibler, 1991]. They are commonly seen in land-fast ice, consolidated ice or a single but large FY ice floe. A crack can appear in reply to wind or tidal force which causes a division of an ice sheet/floe or fractures fast ice. (Fig 1.2).

A crack is any fracture in an ice cover that is generally less than 1 m expanded but a lead is any opening navigable by surface vessel [MANICE, 2005]. Crack also defines as “Any fracture of fast ice, consolidated ice or a single floe which may have been followed by separation ranging from a few centimeters to 1 m” [Sea ice Nomenclature March 2014] (Fig 1.2).

Fig 1.2 left shows the Polarstern in a middle of a crack/lead as it drifted with the sea ice about 260 kilometers from the North Pole on 11 March 2020 (aerial photograph acquired via drone by Manuel Ernst). Right shows the same crack (the photo acquired from board of Polarstern by Steven Fons, a PhD candidate at Maryland and NASA)

1.4.1.2 Leads

Leads are defined as "any fracture or passage-way through sea ice which is navigable by surface vessels"[Sea ice Nomenclature March 2014]. Leads are produced from cracks or fissures (a crack with considerable length and depth) as they open up increasingly under synoptic-scale weather and oceanic patterns. They are the most frequent form of large-scale deformations induced by ice divergence. Leads are normally noted within pack ice or between pack ice and land. They can often branch or intersect, creating a complex pattern of linear features. If leads are produced between floating pack ice and fast ice, they named flaw leads. These are typically noted in the Eurasian Arctic area. Pärn and Haapala [2011] examined their frequency of occurrence in the Gulf of Finland during the period 1971–2007. If a lead lies between the shore and the pack ice, it named a coastal lead. Besides to providing navigational paths to marine vehicles, they have a distinct impact on the heat exchange between ocean and atmosphere. While the ice sheet behaves as an insulator between ocean and atmosphere, leads increase the heat flow to the much colder atmosphere in winter in the polar areas. Correspondingly, although leads generally served as only a few or at most several percent of the ice pack area, they may regard as half of total heat flux from the ocean to the atmosphere [Ruffieux et al., 1995] (Fig 1.2).

Structures of leads in Arctic sea ice are observed over all ranges from aerial photographs to satellite images — directing to self-similar characteristics (or a fractal structure) of sea ice. This impression is supported by the foe size distribution following a power-law scaling (Rothrock & Thorndike, 1984). Power-law scaling was also noted in lead width distributions (Lindsay & Rothrock, 1995), in fracture and faulting of sea ice (Weiss, 2003), and in sea ice deformation (Marsan et al., 2004; Rampal et al., 2008; Stern & Lindsay, 2009) (Fig 1.3).

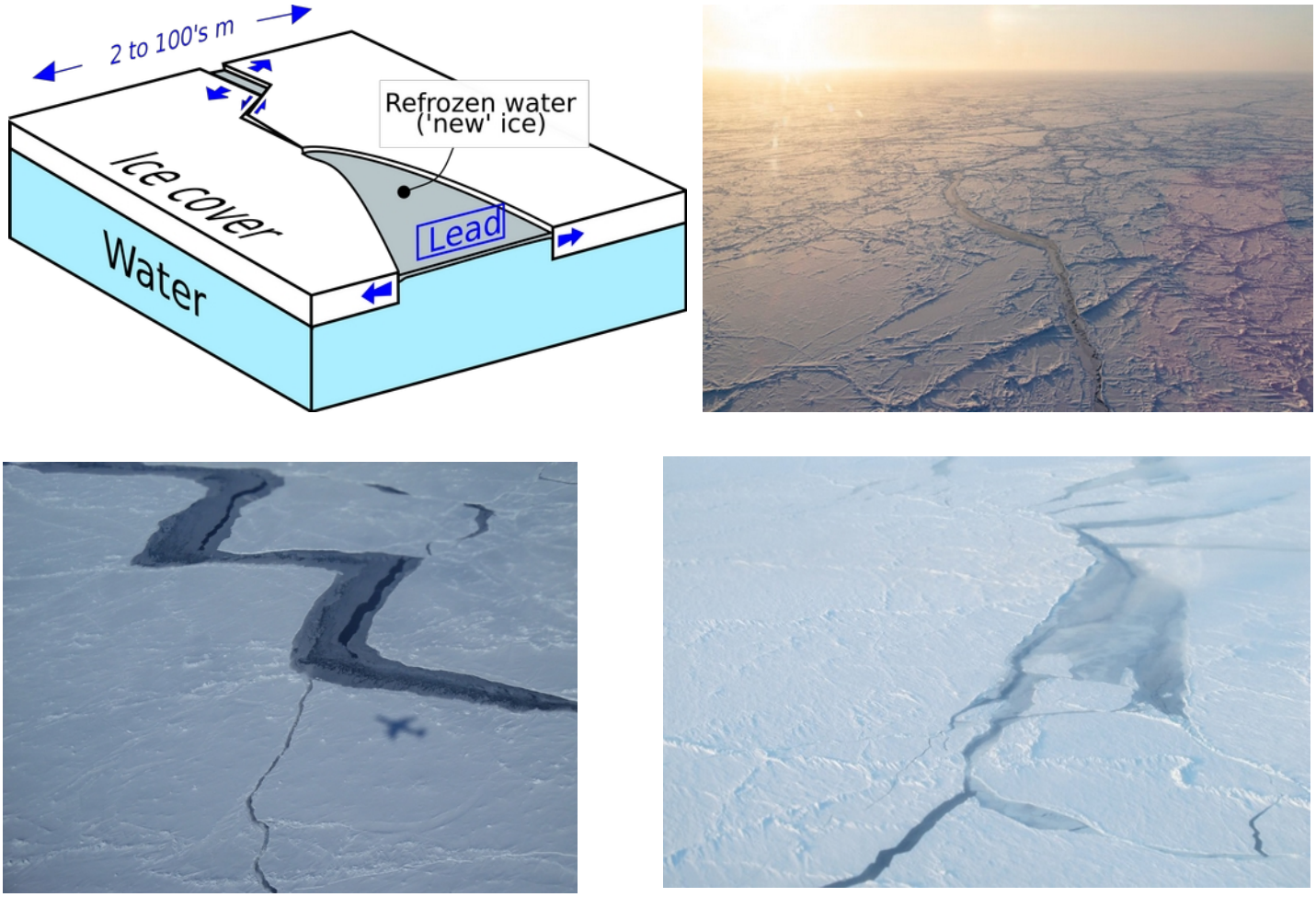

Fig 1.3 Upper left shows schematic image of a lead forming in a sea ice cover. This sketch presumes very low air temperatures, with very fast refreezing of the water inside the lead (Wikipedia). Upper right is a lead located through a network of ridges in the Arctic sea ice pack (MOSAiC area) (Photo by Steven Fons). Lower left and right are also example of Leads by NASA

1.4.1.2.1 Why leads matter

It has been estimated [Maykut, 1982] that half of the total ice production during the winter can happen in leads that cover only 1% of the total area.

Seasonal ice production in ice fractures considers for 25–40% of the total ice growth of the Arctic Ocean.

While a lead opens in the ice during winter, comparably warm ocean waters are uncovered to the cold atmosphere developing in heat fluxes of up to 600 W/m^2 (e.g., Maykut, 1986; Andreas and Murphy, 1986). Accordingly, a plume of warm, moist air produced over the lead, sometimes producing in ice fog, which considerably decreases visibility and can cause ice to accumulate on surfaces such as aircraft, power lines, and roads (e.g., Gultepe et al., 2015).

The brine rejection (salt rejection) from new ice in leads contributes in maintaining of the Arctic ocean halocline and also governs secondary circulation arrangement in the upper ocean (Morison et al. 1992).

The extend of thin ice and open water is also crucial for the total melting during the summer. This is because the nearly black surface of these regions, with low albedo, gives a large absorption of short-wave radiation. Essentially, small areas of thin ice and open water govern the thermodynamic characteristics of the pack as a whole.

Open leads have a low albedo in comparison to the neighboring ice. Nevertheless, in the Arctic winter, the very huge temperature difference between the atmosphere (generally less than −30°C) and the ocean (at freezing temperature of −1.8°C (for surface ocean water)) forces the lead to freeze very quickly. The temperature gradient between newly opened lead and the atmosphere can be so high that the lead “steams” with frost smoke. This is fog-like clouds produce by the contact of colder air with relatively warm water when evaporated water condensates rapidly above the surface. It consists of tiny crystals of ice and may persist while ice cover is producing. This turbulent heat and mass transfer from leads to the atmosphere during winter influences atmospheric procedures hundreds of meters above and hundreds of kilometers downstream from leads (Shokr and Sinha, 2015).

In the central Arctic, leads cover 1%–2% of the surface area in winter and a somewhat higher percentage during the summer. The influence of leads on the ice enclosing is different in winter than in summer. In winter, the open water in the polar leads begins to freeze almost very quickly while exposed to the cold atmosphere and becomes fully frozen within a day or a few days. Correspondingly, the surface of leads generally freezes quickly and becomes covered with thin ice types (e.g., Nilas or gray ice). This leads to a considerable rise in upward turbulent flux of sensible and latent heat. In the summer, the lower albedo of the water surface in leads produces more absorption of solar energy than

the surrounding ice, which fasten the melting of the ice. Open leads discharge moisture to the atmosphere when their freezing discharges heat (Shokr and Sinha, 2015).

Leads also act as navigable marine routes even if they are enclosed with thin ice. Additionally, they are crucial for wildlife. Seals, whales, polar bears, Antarctic penguins, and other animals depend on leads for access to oxygen and food. Currently, the remote sensing community has developed more interest in identification of leads in the Arctic ice since they become more likely to happen as a result of ice thinning. In addition, leads have become the fundamental means for finding out the sea ice free-board needed to estimate ice thickness from airborne and space-borne altimeters [Kwok and Cunningham, 2008; Farrell et al., 2009, Onana et al., 2013]

1.4.2 Rafting, Pressure ridging and Shear ridging

Rafting and pressure ridging are the most routine structures of ice compression at small (Small-scale deformations range from a few hundred meters to a few kilometers) and medium (Medium-scale deformations are defined by a spatial scale that extends a few tens of kilometers) deformation scales.

They contribute to the rising of ice thickness. They happen while two ice sheets are pushed against each other (Fig 1.4). As a rule of thumb, if the sheets are thin rafting is more likely to occur and if they are thick, a pressure ridge will form (Shokr and Sinha, 2015).

Shear ridging, on the other hand, happens while a floating ice sheet moves along the edge of fixed ice (e.g., fast ice) (Shokr and Sinha, 2015).

The local arrangements of pressure ridges gives data on the intensity and frequency of deformation procedures and is a calculation of sea-ice roughness (Shokr and Sinha, 2015).

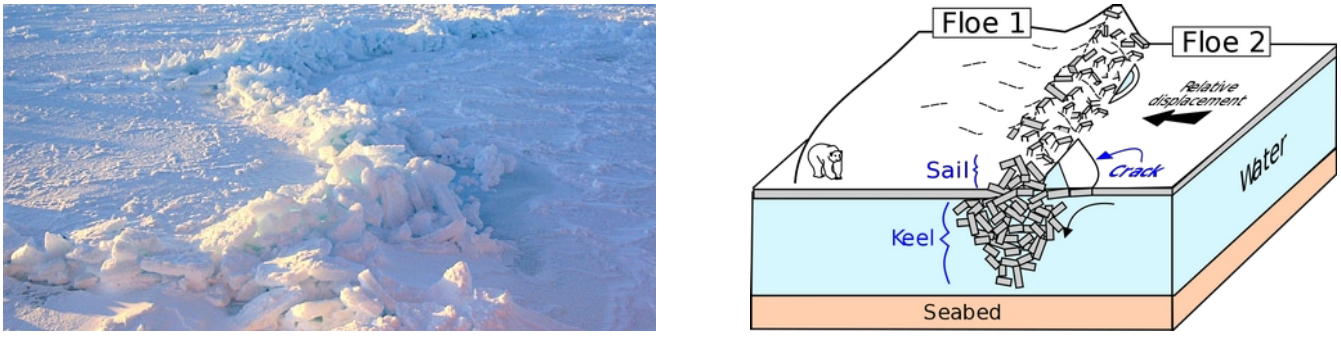

Fig 1.4 left shows a pressure ridge (NASA), right illustrates a hypothetical interaction between two floes, leads to a pressure ridge (Wikipedia).

2 | Methodology

The aim of methodology in this study is to determine deformation parameters from sequence of SAR images. It can be done in two phases (Fig 2.1). At First, an ice drift retrieval should applied. Then, In principle, the deformation of sea ice in the time, Δt, between image acquisitions can be derived from the calculated velocity field. This is usually done by calculating the invariants of the strain-rate tensor from the partial derivatives of the velocity field (Thorndike and Colony, 1982). For the first step, An open-source algorithm from NERSC, Norway is used. It will be explained in detail in section 2.1. For the next, author develop and implement his own algorithm based on the method used by Lindsay et al., 2003. The detail will explained in section 2.2.

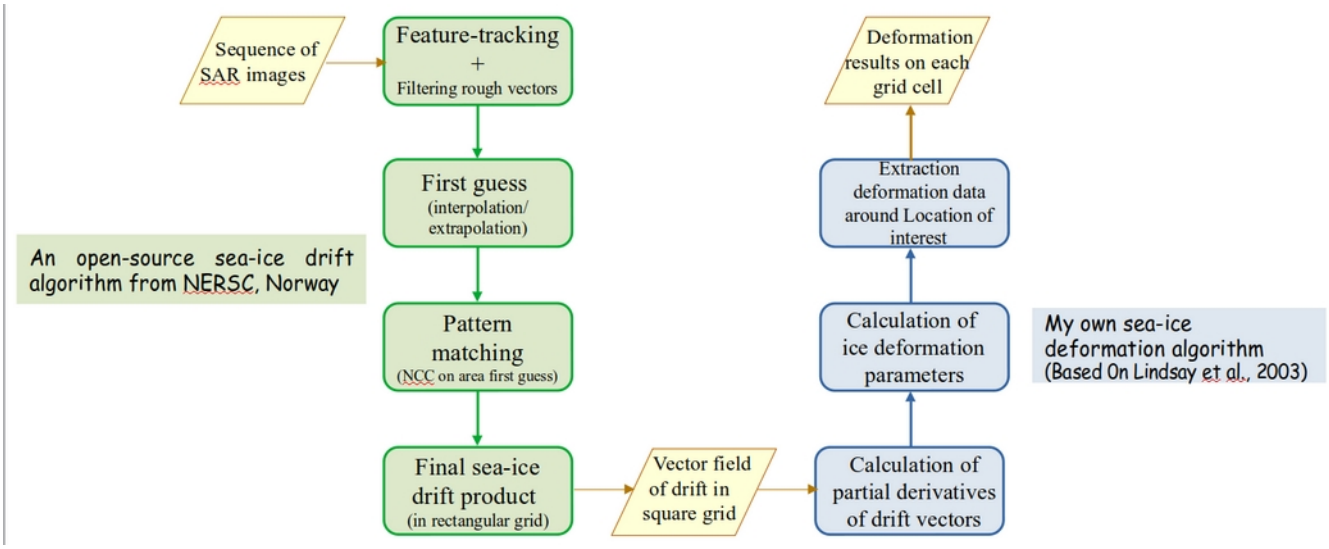

Fig 2.1 shows a flowcharts that describe the algorithms, green is the open-source drift detection algorithm from NERSC, Norway and its steps, blue is my own written algorithm implementing formulas and explanation of Lindsay and Stern (2003) and its main phases and finally yellow represents input and output of both algorithm.

2.1 Sea ice drift algorithm

The algorithm is exploited for detecting sea ice motion in this study is established by combination of a feature tracking and a pattern matching approach. The input of the algorithm are SAR images and the output are ice drifts (in two component: eastward and northward), maximum normalized cross-correlation, and angle of ice rotation. The concept behind this combination is that feature tracking produces a primary estimation of patterns displacement and therefore confines the searching zone for the consecutive pattern matching.

The algorithm that is applied in this thesis paper is developed by Korosov and Rampal (2017) (The algorithm is ready to use in GitHub as free open source package).

2.1.1 Feature-tracking

Generally, a feature-tracking algorithm finds features (a vivid/distinct pattern) at the first stage. To achieve this, it exploits approaches such as segmentation, classification, edge detection. Then it matches the found features between two images and connects similars.

The feature-tracking approach applied by Korosov and Rampal (2017) established on an open-source algorithm called "**O**riented FAST and **R**otated **B**RIEF" (ORB) developed by Rublee et al. (2011). Muckenhuber et al. (2016) adjust it to retrieve sea ice motion form Sentinel-1 SAR images .

ORB detects rotated and scaled features. ORB is a mix of keypoints detector called "**F**eatures from **A**ccelerated **S**egment **T**est" (FAST) (Rosten and Drummond, 2006) and a binary descriptor named "**B**inary **R**obust **I**ndependent **E**lementary **F**eatures" (BRIEF) (Calonder et al., 2010) (which describe patch around the key-point) and it have many adjustments (e.g., FAST does not include orientation, but the ORB algorithm add direction to each key-point using the intensity-weighted centroid from Rosin (1999) that empower the feature-tracking approach to retrieve rotation (in our case only 3 º steps clockwise or counter clockwise) (Rublee et al., 2011) or the BRIEF operate weakly in the case of rotation)

In the feature-tracking phase, the algorithm finds features automatically on the two images and afterwards assign each feature as 256 binary descriptors vector. The procedure describes broadly by Muckenhuber et al. (2016). To find the matched feature, each feature of the first image is compared with all features of the second feature (brute forcing). Hamming distance is exploited to do this comparison. The algorithm computes the ratio between the smallest and the second smallest distance for each feature and then check it with a certain threshold and if the ratio is below the the threshold then it is recognized as matched. Choosing suitable threshold in measuring distance allows us to remove improper matches as much as possible, while accepting almost all proper matches. In the algorithm Korosov and Rampal (2017) use 0.7 as threshold. To detect features efficiently, it is important to detect features in various scales, so the algorithm searches for the features on several pyramid levels (In image processing, the process in which an image is subjected to frequent smoothing and sub-sampling named pyramid approach and pyramid level dictate the number of repetition of exploiting pyramid approach). To describe the range and increment of feature detection scaling, it is

essential to combine number of pyramid levels with the scale factor (A scale factor of 2 means that each next pyramid level has four times fewer pixels). A resolution pyramid with seven steps combined with a scaling factor of 1.2 is suggested by Muckenhuber et al. (2016) and used in the algorithm. Muckenhuber et al. (2016) also determined a patch size of 34 × 34 pixels is proper size for the trade off to have high resolution drift and low computational load. The algorithm uses the same size patch.

The result of this stage are vectors that start from point x_1, y_1 in the first SAR image and end at point x_2, y_2 in the second image (real geographical point, but it is also possible to have this points on images coordinates) with corresponding rotation values α_{raw} (here only 3 degrees in both clockwise and counter clockwise).

Implementation of this method gives us an efficient computational effort. Additionally, retrieving drift vectors are independent of their neighbors (Considering many factors such as position, length, direction and rotation) (This is one of feature tracking advantage against cross correlation method). This is definitely important advantage for resolving shear zones, rotation and divergence/ convergence zones (as main goal of this thesis). The drawback of this method is, it is not typically possible to control the arrangement of result because it depend on location of detected features which are successfully matched by the algorithm (it is not possible to determine result at any location of interest). This drawback can result a large gap between areas which densely covered by (feature-tracking derived) drift vectors (Some area could have a large number of matched feature (so drift result) and some low density result area). This can be problematic because it results missing shear and/ or divergence/ convergence zones (Muckenhuber, et al., 2016). Despite of all, feature tracking methods provide results with low computational load, high degree of accuracy, independent from illumination condition and invariant to rotation of features (Muckenhuber et al., 2016).

2.1.2 Filtering

Feature-tracking produces two coordinate: (i) (x_1, y_1) as coordinates of a feature in the first image (starting point of drift vectors) and (ii) (x_2, y_2) as coordinates of matched feature in the second image (ending point of drift vectors).

Identifying unreliable vectors is next step. two filters are applied on the result vectors in this step. At first, the algorithm filters all drift vectors larger than 0.5 $m.s^{-1}$ as incorrect and then it estimates the value of x_1 and y_1 using the second order polynomial function of x_2 and y_2 computed by the least square

approach and if the simulated starting points are 100 pixels (8 km) far from actual one they will be discarded (remove vectors that do not fit the model $(x_1,y_2)=f(x_2, y_2)^n$, here n=2).

2.1.3 First Guess

Results of feature-tracking are distributed unevenly which make it unpractical but it is really useful because it can be helpful to produce estimation of drift. To do so an interpolation and extrapolation are applied on results (linear barycentric interpolation) which construct first guess of results. The quality of this estimation depends on the density of the feature-tracking vector field and the local ice conditions. Finally, this step provides x_2, y_2 and α (guessed location and rotation (only for 3 degree clockwise and 3 counter-clockwise) on image two) at any location of image one.

2.1.4 Pattern matching

As final stages, a pattern matching applied on images (here, only the applied pattern matching method will be explained for other methods see appendix A). Pattern-matching is now really efficient because the search area is confined by result of the first guess. This method is established on measuring similarities between a pair of images. First, a template (a 2-D image which is normally a tiny part of image) from the first image is chosen. Second, it searches for its (best) match by sliding the template throughout the second image. This approach is a computationally heavy (but it is still extensively used because user can calculate result in any location of interest). A common approach to decrease the computational load is exploiting a speed up processes such as pyramid approaches. This approach plus the first guess results reduce the searching area. The most common approach for pattern-matching is "Maximum Cross Correlation" (MCC) method (For other approaches and detail of this method see Appendix A). First, for the point of interest, a small template around the point of interest t_1 with the size $t_1 \times t_1$ should be chosen. Then it slides on a larger template t_2 with the size $t_2 \times t_2$ at the guess point on the image two (x_2, y_2). So then the algorithm calculates the matrix of "Normalized Cross Correlation" (NCC). To consider the possible rotation of patch, the algorithm repeats sliding and calculating NCC for different angles (in the algorithms, it is limited to for 3 º clockwise and 3 º counter-clockwise (to maintain efficiency of computational load)). This approach returns the NCC matrix with the highest cross-correlation value as output.

Korosov and Rampal (2017) applied a sensitivity test and also recommend value for both t_1 and t_2 based on polarization and distance from closest matched featured.

2.1.5 Final drift product

Korosov and Rampal (2017) found that the value of the MCC_{max} is inversely proportional to retrieval error E for both polarization HH and HV channels (Retrieval error E is distance between the buoy GPS position and retrieved location of ice in the second image). So they ended to choose a MCC_{min} as filter to removing vectors with too low MCC. They advise MCC_{min} value as 0.3. It is an optimal value that keeps most vectors (85% for HH and 95% for HV) with the highest accuracy. Korosov and Rampal (2016) state that " if MCC_{min} is reduced, an additional rogue-vector detection procedure needs to be applied (Barton, I.J, 2002)".

Finally, the algorithm can provide drift displacement, mean velocity, Correlation and angle of rotation. Fig 2.2 shows location of an example case study with an example of its feature tracking and its pattern matching result. Fig 2.3 is variety of results for that two SAR images on 24 and 27 December 2017 used in Fig 2.2.

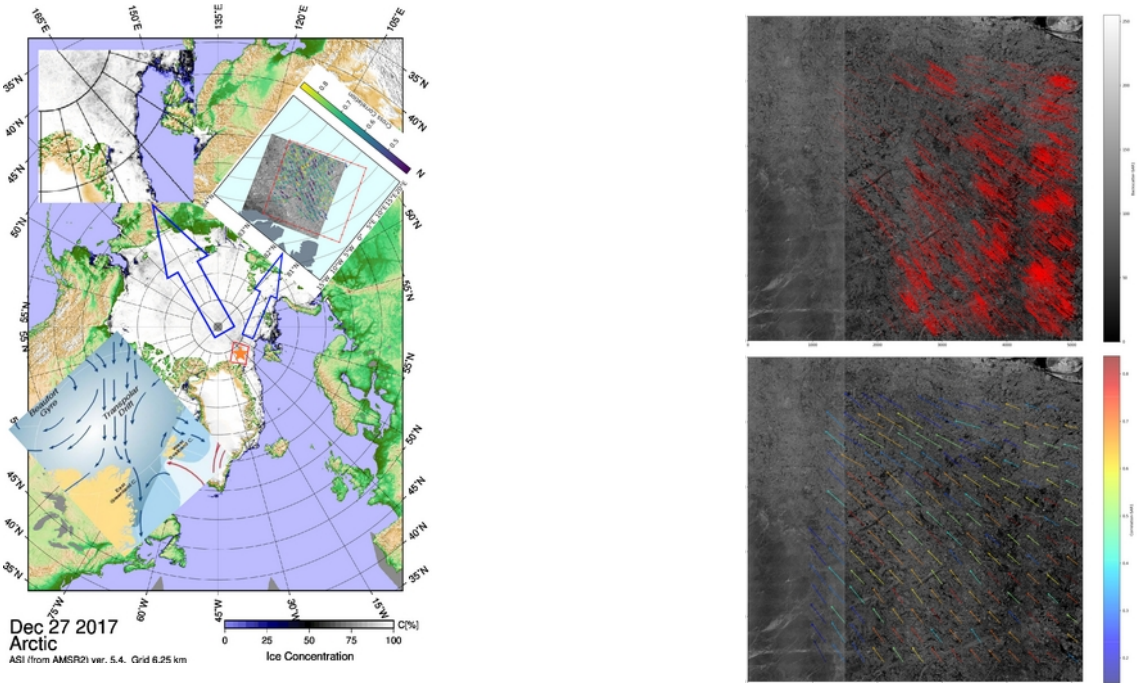

Fig 2.2 shows an example result of the open-source sea ice drift algorithm for the two SAR images ob 24 and 27 December 2017, left shows the location of SAR images, general pattern of ocean current at that location and SIC (**S**ea **I**ce **C**oncentration) on 24 December 2017 (IUP Bremen – Remote sensing of polar regions group), upper right and lower right show an example of feature-tracking and final result of drift detection algorithm respectively.

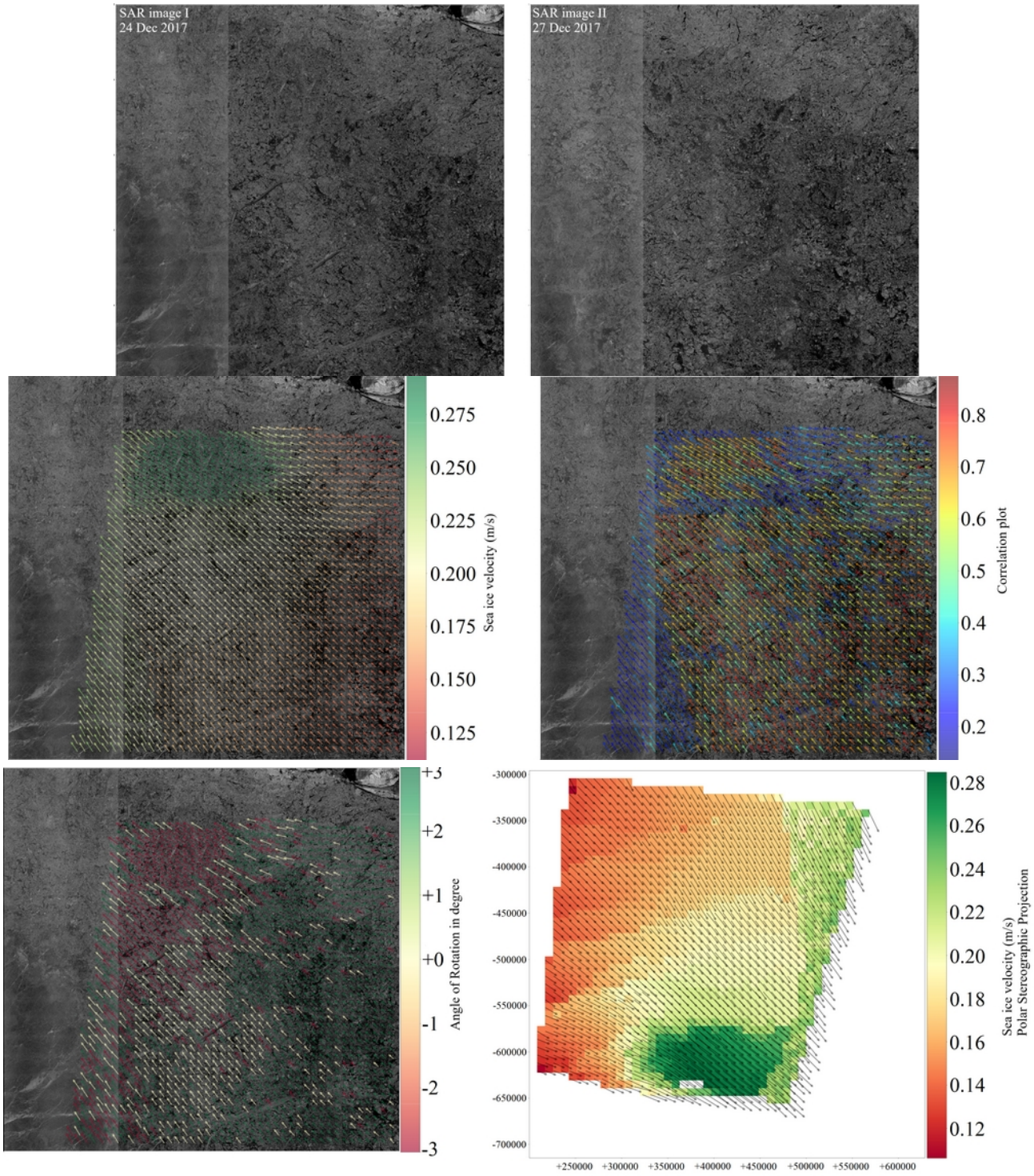

Fig 2.3 shows example of drift detection products (between 24 and 27 December 2017 in North-east of Greenland) which row by row and left to right are SAR image on 24 Dec, SAR image on 27 Dec, sea ice mean velocity, correlation of sea ice drift, rotation of angle of sea ice drift and sea ice velocity in stereo-graphic projection respectively.

2.2 Sea ice deformation algorithm

As part of this thesis, a deformation module was implemented by author which its methodology will explained as follow.

The strain rate of the ice appears from spatial inconsistency of the velocity of sea ice, while the velocity components u and y are calculated from the displacement components and the time interval between the SAR images. The spatial gradient in the velocity field has two invariants (invariant with respect to coordinate system): divergence and shear. Another output is vorticity. These are calculated from the components of the strain rate tensor (Rothrock, 1986):

$$Divergence = \frac{\partial u}{\partial x} + \frac{\partial v}{\partial y} \tag{2-1}$$

$$Shear = \left[\left(\frac{\partial u}{\partial x} - \frac{\partial v}{\partial y} \right)^2 + \left(\frac{\partial u}{\partial y} + \frac{\partial v}{\partial x} \right)^2 \right]^{1/2} \tag{2-2}$$

$$Vorticity = \frac{\partial v}{\partial x} - \frac{\partial u}{\partial y} \tag{2-3}$$

To measure of the total sea-ice deformation rate following formula is exploited:

$$Total\ deformation = \sqrt{Shear^2 + Divergence^2} \tag{2-4}$$

which is exploited as a measure for the general ice deformation happening at a specific position in space (e.g., Stern and Lindsay, 2009).

The derivatives are computed with the line integral around the edges of a grid cell. To do so, grids require to be determined, while each grid vertex serves as the basis of a drift vector. For this purpose, drifts vector are computed in a regularly distributed of grid of squares.

The partial derivatives of the drift vector field are calculated from a line integral, which for discrete values is approximated by using the trapezoidal rule (Lindsay et al., 2003):

$$\frac{\partial u}{\partial x} = u_x = \frac{1}{A} \oint u\, dy \simeq \frac{1}{2A} \sum_{i=1}^{n} (u_{i+1} + u_i)(y_{i+1} - y_i) \tag{2-5}$$

Here for grid of squares:

$$\frac{\partial u}{\partial x} = \frac{1}{2A} \left\{ \left[(u_2 + u_1)(y_2 - y_1) \right] + \left[(u_3 + u_2)(y_3 - y_2) \right] + \left[(u_4 + u_3)(y_4 - y_3) \right] + \left[(u_5 + u_4)(y_5 - y_4) \right] \right\} \tag{2-6}$$

$$\frac{\partial u}{\partial y} = \frac{1}{2A} \left\{ \left[(u_2 + u_1)(x_2 - x_1) \right] + \left[(u_3 + u_2)(x_3 - x_2) \right] + \left[(u_4 + u_3)(x_4 - x_3) \right] + \left[(u_5 + u_4)(x_5 - x_4) \right] \right\} \tag{2-7}$$

$$\frac{\partial v}{\partial x}=\frac{1}{2A}\left\{\left[(v_2+v_1)(y_2-y_1)\right]+\left[(v_3+v_2)(y_3-y_2)\right]+\left[(v_4+v_3)(y_4-y_3)\right]+\left[(v_5+v_4)(y_5-y_4)\right]\right\} \quad (2\text{-}8)$$

$$\frac{\partial v}{\partial y}=\frac{1}{2A}\left\{\left[(v_2+v_1)(x_2-x_1)\right]+\left[(v_3+v_2)(x_3-x_2)\right]+\left[(v_4+v_3)(x_4-x_3)\right]+\left[(v_5+v_4)(x_5-x_4)\right]\right\} \quad (2\text{-}9)$$

(x_i, y_i) are the locations and (u_i, v_i) the velocity components for n points (here as square, n=4) forming the boundary of a region (the indices increase when proceeding counter-clockwise around the cell and $x_{n+1} = x_1$, $y_{n+1} = y_1$ (here, $x_5 = x_1$, $y_5 = y_1$), etc.)

The area is computed as

$$A=\frac{1}{2}\sum_{i=1}^{n}\left(x_i y_{i+1}-y_i x_{i+1}\right) \quad (2\text{-}10)$$

Here for grid of squares:

$$A=\frac{1}{2}\left[(x_1 y_2-y_1 x_2)+(x_2 y_3-y_2 x_3)+(x_3 y_4-y_3 x_4)+(x_4 y_5-y_4 x_5)\right] \quad (2\text{-}11)$$

(x_i, y_i) are the locations for n points (here as square, n=4) forming the boundary of a region (the indices increase when proceeding counter-clockwise around the cell and $x_{n+1} = x_1$, $y_{n+1} = y_1$ (here, $x_5 = x_1$, $y_5 = y_1$), etc.). because we use fixed uniformed squared grid its value is fixed (e.g., for spatial resolution of 800 × 800 m, it is equal to 640,000 m^2).

Finally, the algorithm can provide deformation parameters: divergence, shear, vorticity and total deformation. Fig 2.4 is an example results for two SAR images on 24 and 27 December 2017 in North-east of Greenland.

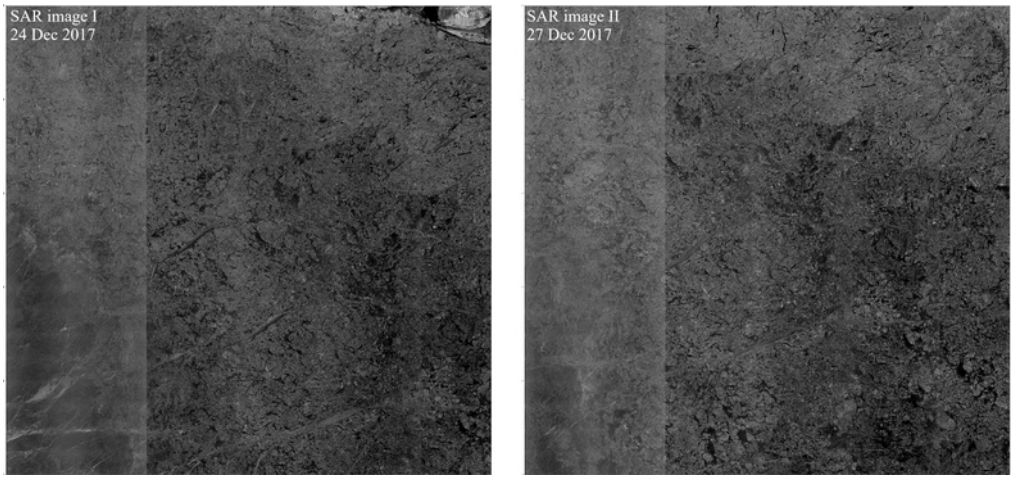

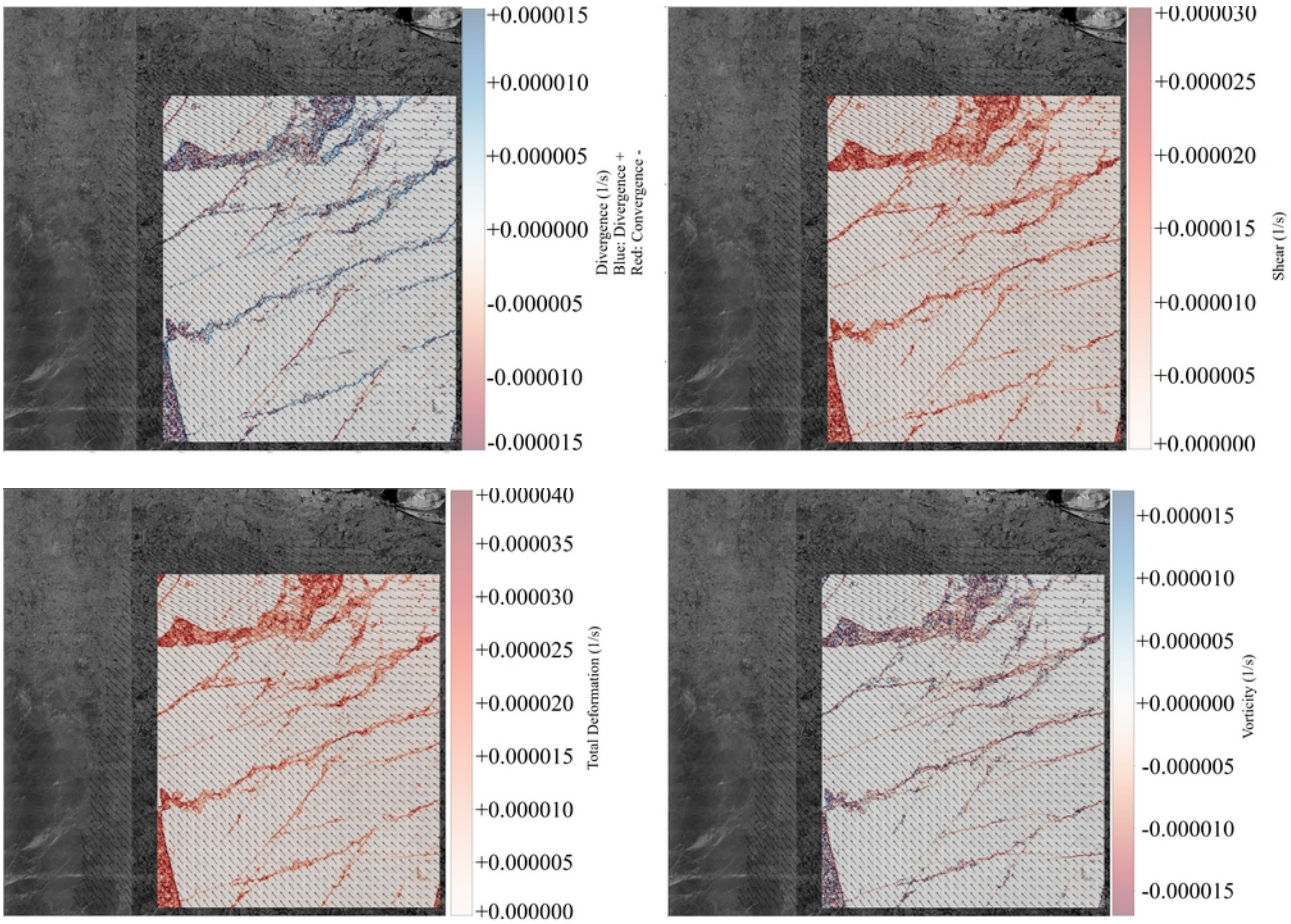

Fig 2.4 shows example of deformation retrieval products (between 24 and 27 December 2017 in North-east of Greenland) which row by row from left to right are SAR image on 24 Dec (page 29), SAR image on 27 Dec (page 29), result for sea ice mean divergence, shear, vorticity and total deformation respectively (see Fig 2.3 for the drift result).

3 | Data and case study

The Sentinel-1 mission (Fig 3.1) is a joint initiative of the European mission and the "European Space Agency" (ESA) and serves as the European Radar Observatory for the Copernicus programme, a European system for observing the Earth for the environmental and security matters. It involves two completely similar satellites, Sentinel-1A (launched in April 2014) and Sentinel-1B (launched in April 2016). The sensor for the two satellites, is a single C-band SAR (center frequency: 5.405 GHz). It supports dual-polarization (HH + HV, VV + VH) also for the wide swath mode. The satellites orbit in the identical near-polar, sun-synchronous orbit with a revisit time of less than 1 day in the Arctic (altitude: 693 km, Inclination: 98.18º and period: 98.6 minutes) (ESA, 2012) (See table 3.1).

Our algorithm for sea ice motion exploits the Extra Wide mode at Ground Range Detected Medium Resolution (EW GRDM). In this mode, an region of 400 km × 400 km is covered by one image with a pixel spacing of 40 m × 40 m (resolution: 93 m range × 87 m azimuth) for both HV (horizontal transmit, vertical receive) and HH (horizontal transmit, horizontal receive) polarizations (Number of looks (range × azimuth):(6 × 2)). Although the algorithm operates for both polarization, in this thesis, the HV polarization is preferred, because for HV it provides on average four time more vector numbers than HH polarization in feature-tracking stage (Muckenhuber et al., 2016). This means it can provide better estimation of drift in "first guess" phase. Additionally, despite the fact that HV channel is normally noisier than HH channel, Komorov and Barber (2014) detected that noise floor stripes in the HV images do not influence the drift retrieval from pattern-matching. Muckenhuber et al. (2016) developed this argument for their feature-tracking algorithm, so they exploited a noise removal for HV and angular correction for HH and they detected that does not enhance feature-tracking results.

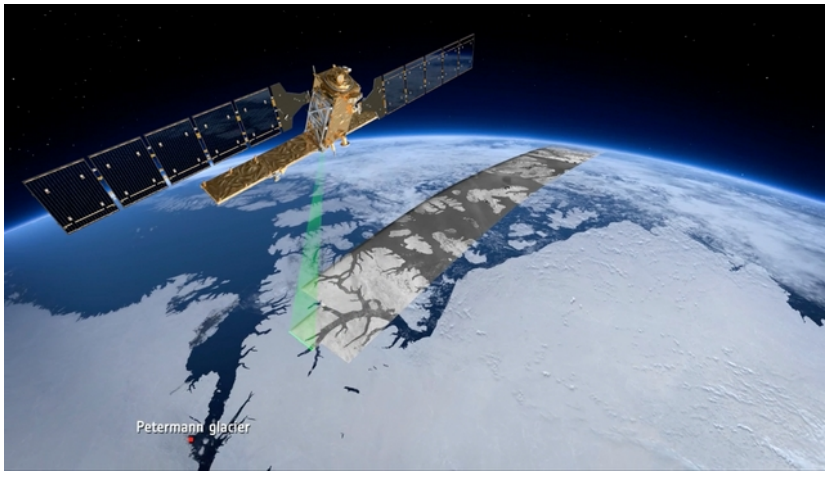

Fig 3.1 shows Sentinel-1 satellite and example of its SAR images (ESA)

Satellite images	Sentinel-1 SAR	Center frequency	5.405 GHz (C-band)
Launch time	Sentinel-1A: April 2014 Sentinel-1B: April 2016	Polarisation	VV+VH, HH+HV
Altitude	693 Km	Repeat cycle	12-day
Oribit	Near-polar, Sun-synchrounous	Launch mass	2300 kg
Inclination	98.18º	Incidence angle	20º - 45º
Period	98.6 min	lifetime	7 years
Revisit time	Less than 1 day (Arctic)	Pixel spacing	40 m × 40 m

Table 3.1 shows Sentinel-1 satellite main characteristic (ESA)

3.1 Why Sentinel-1 SAR data

In the Earth system modeling, grid cells are divided into an ice and an open-water and consider the ice-covered region as an obstruction to heat and gas fluxes. However, observations propose that exchange in cracks and small leads can be much higher in localized areas than anticipated under same circumstances in open water. Marcq and J. Weiss [2012] illustrate that turbulent heat fluxes over sea ice rely firmly upon the lead width (rise in heat flux with fall of lead width) and that the total computed heat flux massively depends on the lower bound (Arctic-wide cloud free lead detection is only possible by satellite SAR images).

As it is independent from cloud and light conditions and it can look through dry snow, SAR is an essential tool for retrieving the drift and deformation structures of sea ice (Dierking, 2013).

Satellite SAR imagery of the sea ice cover has the power of all-weather day-and-night functional capability, fine spatial resolution (10–100 m), good geometric precision, and sensitivity of the radar back-scatter to the roughness, dielectric and physical properties of various sea-ice types and open water (Kwok, 2010).

The most appropriate remote sensing instrument for retrieving of ice surface deformation is SAR. That is partially due to its fine spatial resolution but principally due to its sensitivity to surface roughness and pattern. Actually, this fascinating feature has revolutionized many applications in the fields of geology and Earth’s surface morphology. All shapes of surface deformation at all scales are

linked with some degree of high back-scatter in SAR images in both co- and cross polarization (Shokr and Sinha, 2015).

.
.

3.2 Preprocessing

The essential actions involves 3 steps as follow:

(i) radiometric calibration.

(ii) down-sampling.

(iii) geolocation.

All these are accomplished exploiting Python Nansat package (Korosov et al., 2016) (all essential Nansat functions are implemented inside the algorithm).

3.2.1 Radiometric calibration

The goal of this sub-section is computing normalized radar back-scatter cross-section (σ^0) in dB as eight-bit integer data type. To do so, the algorithm employs the radiometric calibration to **D**igital **N**umbers (DN) and calibration look-up-table (A). This grants us to calculate the normalized radar back-scatter cross-section in dB (digital number is supplied in the TIFF file and calibration look-up-table is provided inside metadata XML files):

$$\sigma^0 = 10log_{10}(DN^2 / A^2) \tag{3-1}$$

The normalized radar back-scatter cross-sections are now in 32-bit floating-point. The algorithm exploits following formula to convert it to eight-bit integer data:

$$\sigma_8^0 = 255\left(\sigma^0 - \sigma_{MIN}^0\right)/\left(\sigma_{MAX}^0 - \sigma_{MIN}^0\right), \left[\sigma_8^0 \in \mathbb{Z} \vee 0 \leqslant \sigma_8^0 \leqslant 255\right] \tag{3-2}$$

where $\sigma_{MAX}^0, \sigma_{MIN}^0$ are minimum and maximum values of σ^0 identified individually for HH and HV polarization.

3.2.2 Down-sampling

To reduce speckle noise (technically, speckle is not noise in its commonly understood sense of an unwanted modification to a desired signal. Rather, it is the signal itself that fluctuates, because the scatterers are not identical for each cell, and the signal is highly sensitive to small variations in scatterers (Moreira et al., 2013)), pixel size reduced by down-sampling to 80×80 using averaging of the nearest pixels. Images were used in swath projection and were not collocated on the same grid (re-projected).

3.2.3 Geo-location

In the supplement metadata files, there are files including the **G**round **C**ontrol **P**oints (GCPs). They are used to transfer the coordinates from the image coordinate system (rows, columns) to the geographical coordinate system (longitude-latitude) and back.

3.3 Case study

The Polarstern drift during MOSAiC expedition was chosen as area of investigation. MOSAiC expedition is the **M**ultidisciplinary drifting **O**bservatory for the **S**tudy of **A**rct**i**c **C**limate expedition. It started on October 2019 and planned to finished on October 2020. During the expedition, a modern research icebreaker, the research icebreaker Polarstern from Germany's Alfred Wegener Institute, Helmholtz Centre for Polar and Marine Research (AWI), will operate in the direct vicinity of the North Pole year round (and especially nearly half year long polar night during winter). As inspiration, the RV Polarstern plays the role of the wooden sailing ship Fram in Fridtjof Nansen's famous expedition in the years 1893–1896, over 125 years ago. His expedition showed the possibility of letting a ship drift across the polar cap (solely driven by the forces of the natural drift of the ice). The primary goal of MOSAiC is to understanding the coupled climate processes in the Central Arctic (to make our global climate model more accurate. It also helps to improve weather forecast and enhance accuracy of Arctic sea ice forecast (Fig 3.2 and 3.3).

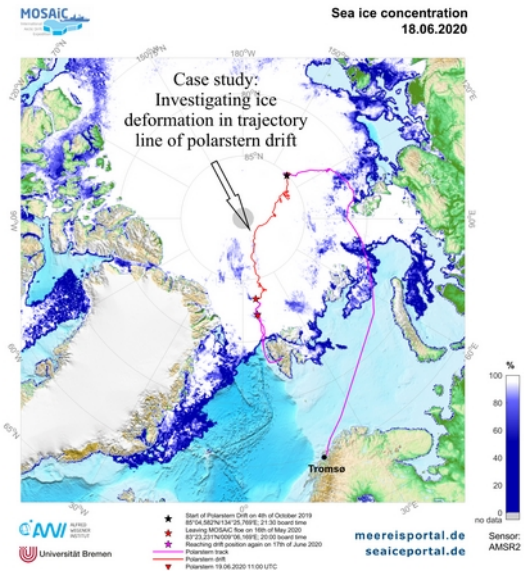

Fig 3.2 left shows an image of German **R**esearch **V**essel (RV) (Photo by Stefan Hendricks – AWI), right illustrates actual drift of Polarstern during MOSAiC expedition up to 18.06.2020 (meereisportal.de)

The trajectory of Polarstern drift during MOSAiC expedition is chosen as case study because it is a good opportunity to compare our results with data of the expedition and interpret its anomalies.

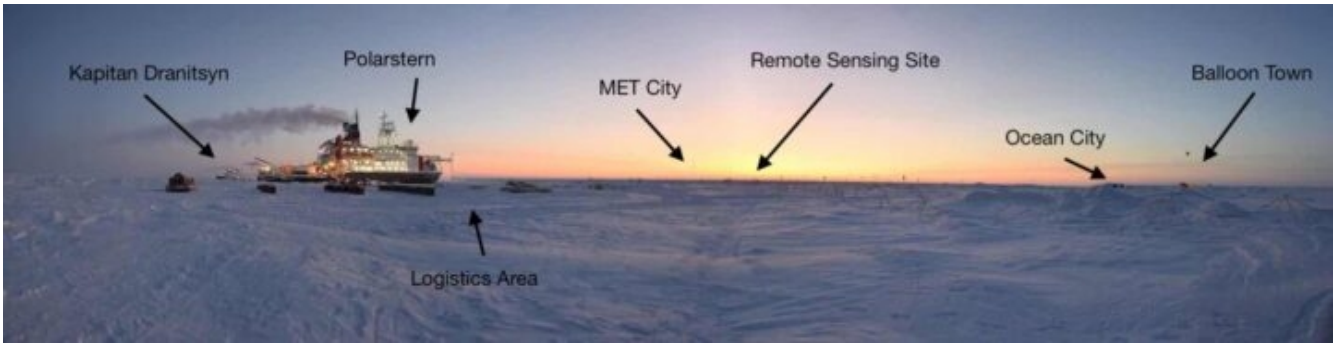

Fig 3.3 The Central Observatory of MOSAiC, with a few prominent landmarks noted. This photo was taken while the Kapitan Dranitsyn was stationed nearby (Credit: Steven Fons (16 March 2020)).

4| Results

Pattern-matching, by nature, grant us to have a user determined ice displacement vector field (In any grid or in irregular positions or even in just a few points of interest). For matter of visualization, we exploit grid with spatial resolution of 8 km × 8 km, but to presenting a meaningful and computationally efficient sea ice deformation results a sea-ice drift with spatial resolution of 800 m × 800 m has been selected in pattern-matching process. The initial result of the sea ice algorithm are drift vectors on each grid cell with corresponding pixel-line coordinates (image one coordinates) and the correlation value (and rotation values which are not shown in the visualization). The drift vectors with correlation value less than 0.3 should not be considered (by recommendation of Korosov and Rampal, (2017)), but for calculation of sea ice deformation, this filter is not considered in retrieval (because they mainly happens in deformation area (locations of ridges and leads) and they may be missed).

To evaluate the algorithm, a sequence of SAR images is chosen. Both images cover approximately same area and location of the research vessel Polarstern at time of acquisition images, So both are located in position of area of interest (MOSAiC expedition). Fig 4.1 shows location of the first image projected on Google map and their situation in MOSAiC expedition.

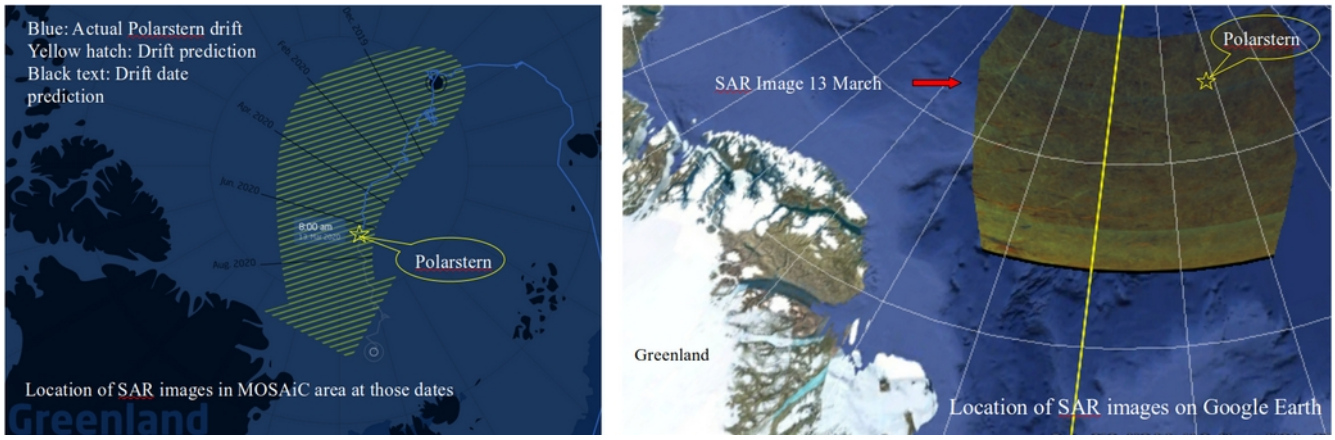

Fig 4.1 shows the location of the two SAR images 13 and 14 March 2020 on MOSAiC drift path (left) and Google Earth projection of it (right) (Credit: follow.mosaic-expedition.org and Google Earth)

Table 4.1 shows date and time of image acquisition and file name of the two SAR images. Both images downloaded freely from "Copernicus Open Access Hub" (https://scihub.copernicus.eu/dhus/#/home).

Name	Date	Time (UTM)
S1B_EW_GRDM_1SDH_20200313T114854_20200313T114954_020673_027304_C177.zip	13.03.2020	11:49:54 AM
S1B_EW_GRDM_1SDH_20200314T105131_20200314T105231_020687_027372_2C73.zip	14.03.2020	10:52:31 AM

Table 4.1 shows characteristic of the two SAR images on 13 and 14 March 2020.

To retrieve deformation parameters from those sequence of SAR image, first we applied the NERSC drift detection. In its pattern-matching step, a squared shaped grid is defined on first SAR image with spatial resolution of 800 m × 800 m. The algorithm retrieved drift results are shown in Fig 4.2 (In the figure, for purpose of visualization a spatial resolution of 8 km × 8 km used).

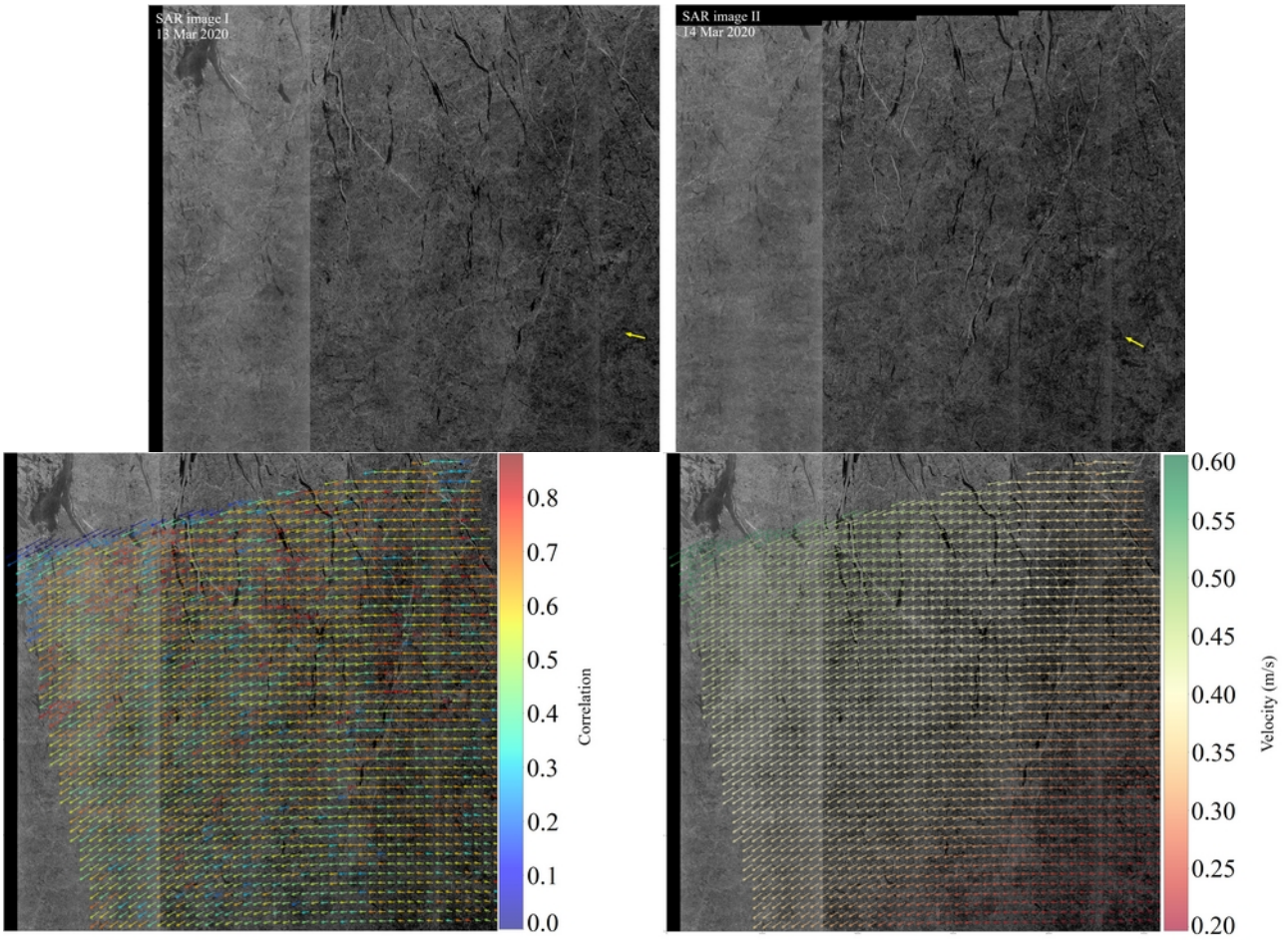

Fig 4.2 shows results of sea ice drift for the two example of SAR image on 13 and 14 March 2020 (first row from left to right), shows correlation result and sea ice velocity in the second row from left to right respectively.

Afterward, based on result drift detection algorithm and time interval between image acquisition of the two SAR images, for each grid point, both components of mean velocity will be calculated (u in x direction of image and v in y direction of image). Now, the input for deformation retrieval is ready and deformation parameters can be calculated for each grid cell (each grid cell contains 4 grid points, deformation formulas were applied on these 4 grid points and results were stored on the center of grid cells).

Deformation results include results for divergence, shear, vorticity and total deformation. Fig 4.3 shows visualization of deformation parameters on the first SAR image (13 March).

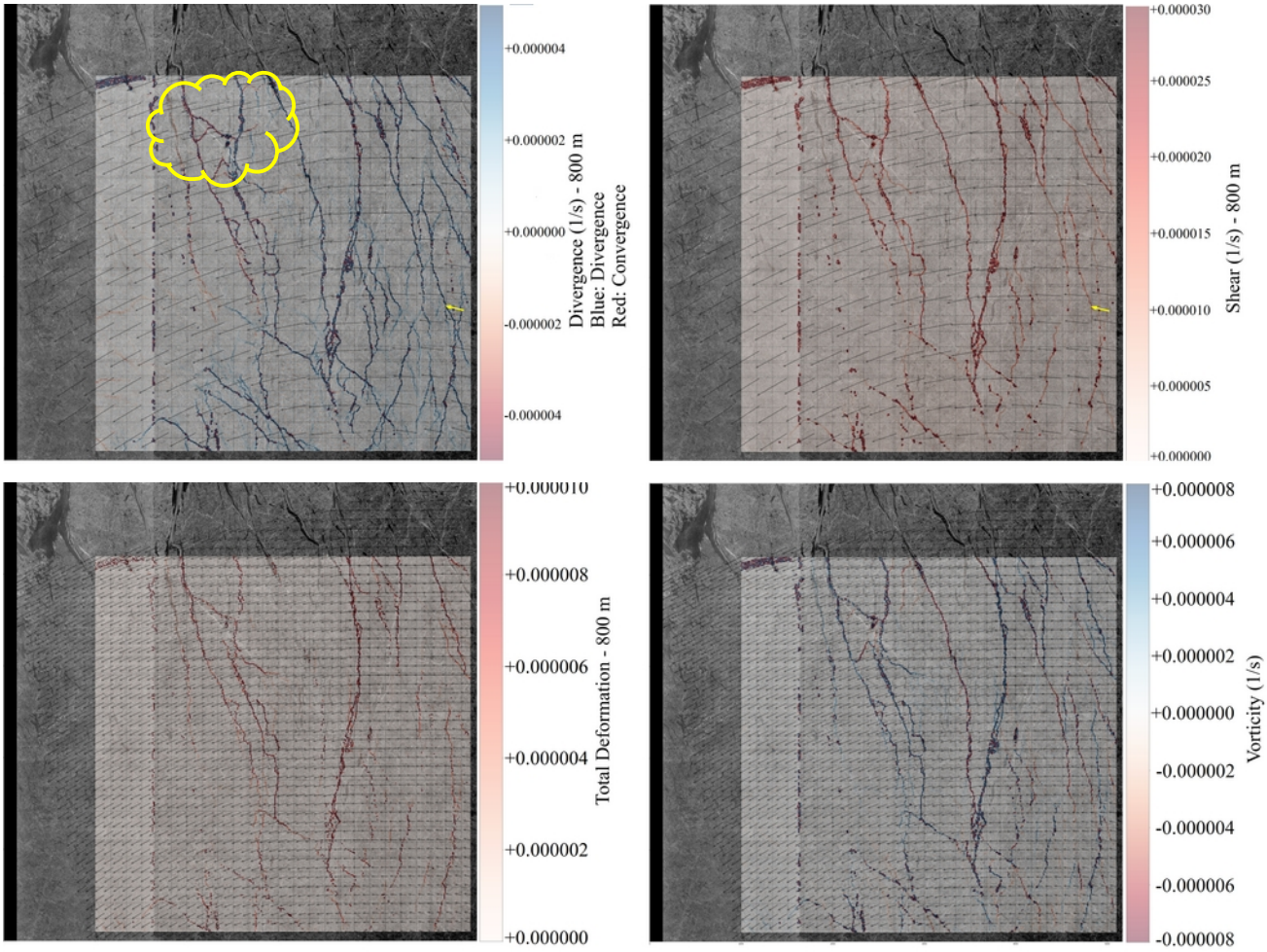

Fig 4.3 shows results of sea ice deformation for the two example of SAR image on 13 and 14 March 2020, from up to down shows divergence, shear, total deformation and vorticity respectively (in each row from right images are the first SAR image, the second and result respectively).

If we zoom in cloudy area on Fig 4.3, we have a lead on 13 March 2020 that become more pronounce in the next day. Fig 4.4 shows application deformation retrieval algorithm on zoomed location. It gives high positive value for the location of lead on the first SAR image (bluish result in visualization). This means we should expect happening of an opening (high value of divergence can lead to an opening) and if we look to the next image (14 March 2020) observer can clearly see the opening visually, so the deformation retrieval algorithm implemented correctly.

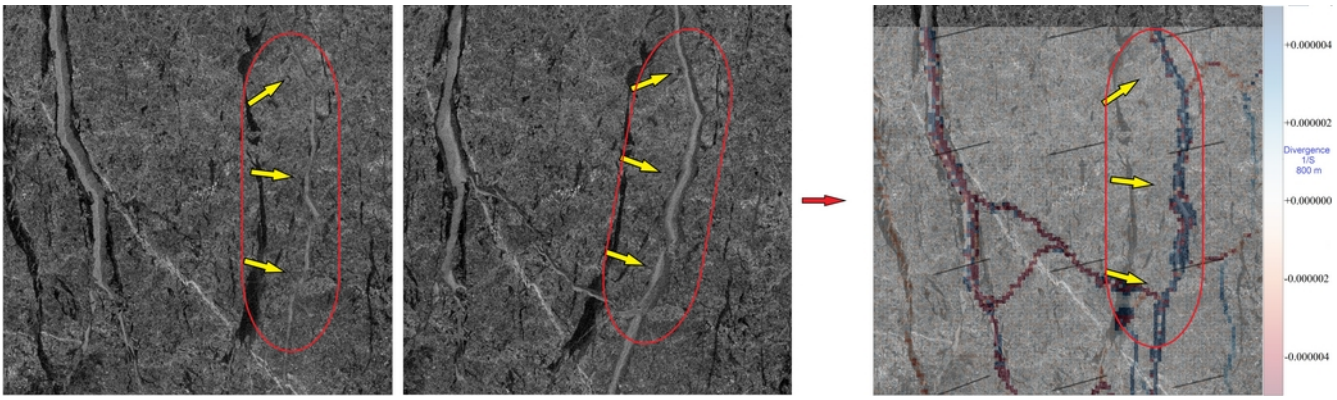

Fig 4.4 shows zoomed location of fig 4.3 in cloud sign directed area to evaluate the algorithms.

Therefore, the algorithm is ready to investigate deformation parameters variations around Polarstern while it was drifting through the Arctic during the MOSAiC expedition in the arctic wintertime. To do so, in each week from 1 October, two SAR images are chosen. These SAR images are chosen carefully based on following criteria: (i) for each consecutive images, location of Polarstern at the time acquisition of both images should be inside the area of both images. (ii) both images should have very good overlap (Polarstern should be inside this overlap area at both time of images acquisition) and (iii) availability results in most part of a hypothetical area around Polarstern (a circle with center in Polarstern location and radius of 50 km).

After choosing proper SAR image (Table 4.2), the algorithm are applied between each sequence of SAR images to calculate sea ice drift and following deformation parameters: (i) divergence, (ii) shear and (iii) total deformation. Then three square shape area (with location of Polarstern is on their center) with edge size of 20, 60 and 100 km are defined to calculate mean value of informed deformation parameters and mean sea ice speed. Fig 4.5 illustrate time-series of deformation parameters and mean ice speed in area around Polarstern during its drift in MOSAiC expedition.

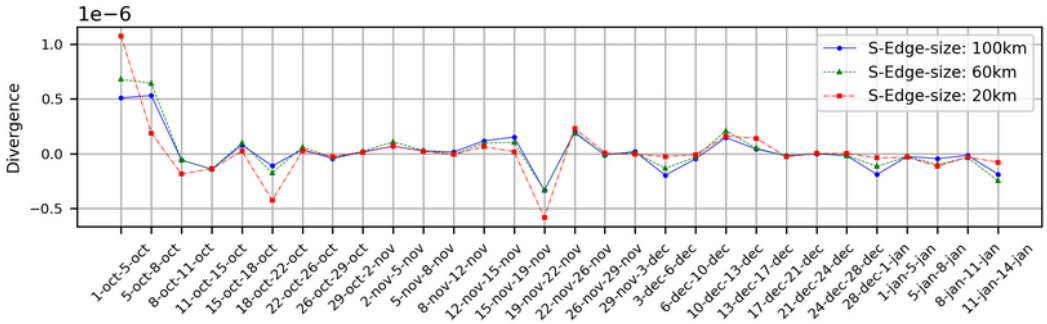

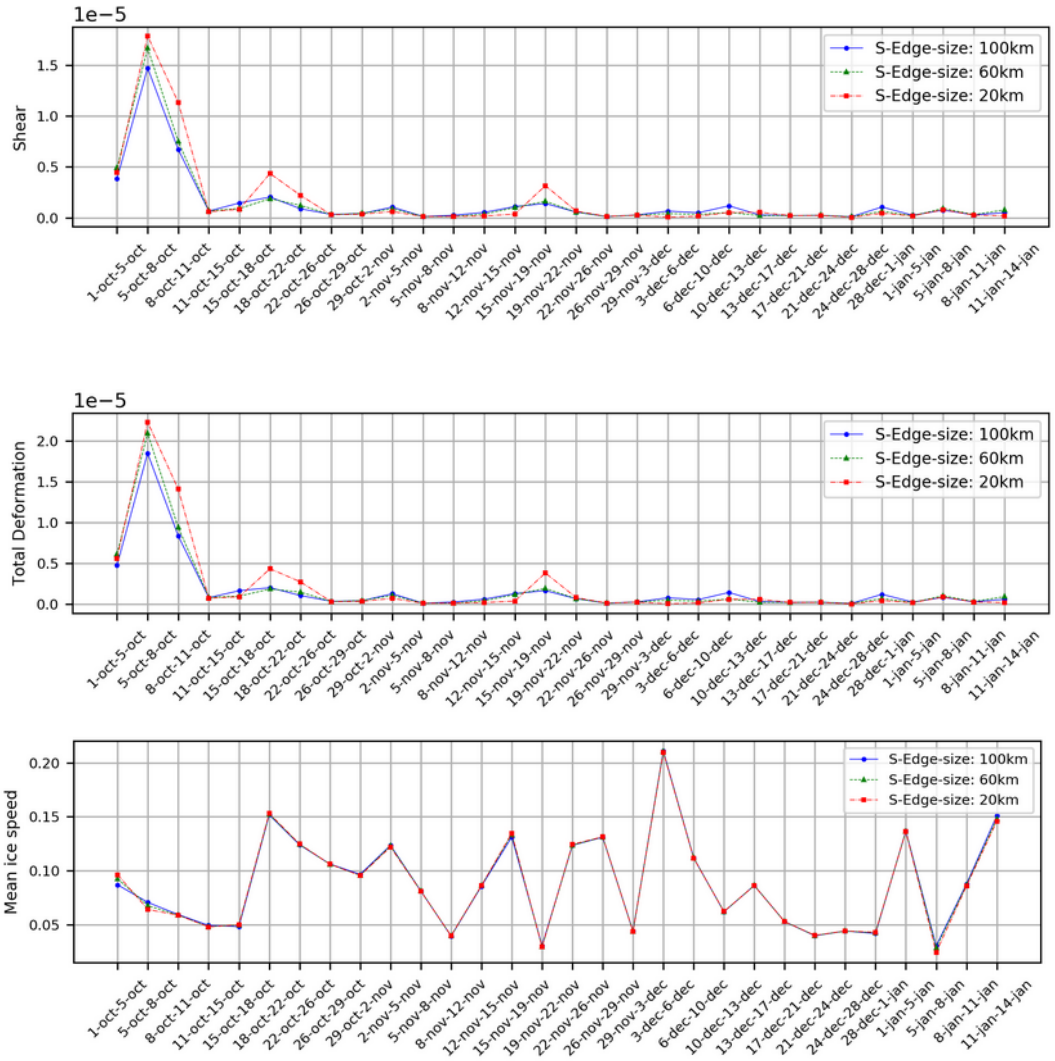

Fig 4.5 shows from up to down time-series of mean value in three size area (edge size of 20, 60 and 100 km) deformation parameters divergence (page 39), shear and total deformation and mean ice speed respectively.

Date	Time (UTC)	Date	Time (UTC)	Date	Time (UTC)	Date	Time (UTC)
1 Oct 2019	05:30:17	2 Nov 2019	03:35:43	29 Nov 2019	04:00:11	28 Dec 2019	04:08:21
5 Oct 2019	05:46:25	5 Nov 2019	04:00:11	3 Dec 2019	03:27:31	1 Jan 2020	03:35:41
11 Oct 2019	04:08:25	8 Nov 2019	04:24:43	6 Dec 2019	03:52:02	5 Jan 2020	04:41:01
15 Oct 2019	06:02:45	12 Nov 2019	05:30:02	10 Dec 2019	03:19:19	8 Jan 2020	03:27:30
18 Oct 2019	06:27:17	15Nov 2019	04:16:31	13 Dec 2019	03:43:51	11 Jan 2020	03:52:01
22 Oct 2019	05:54:37	19 Nov 2019	03:43:52	17 Dec 2019	04:49:10	14 Jan 2020	04:16:29
26 Oct 2019	05:21:54	22 Nov 2019	04:08:23	21 Dec 2019	04:16:30	13 Mar 2020	11:48:54
29 Oct 2019	04:08:23	26 Nov 2019	03:35:43	24 Dec 2019	04:41:01	14 Mar 2020	10:51:31

Table 4.2 shows the list of data used in this study

5 | Discussion and Outlook

Sea ice affects life in the polar regions, but it also is a crucial factor in the climate system due to its interaction with the atmosphere and ocean.

In this study, we exploit an open-source algorithm named “SeaIceDrift-0.6” to retrieve sea-ice drift and develop and implement an algorithm to determine deformation parameters such as shear, divergence, vorticity, and total deformation using partial derivatives of the vector field of velocity (derived from the drift detection algorithm). The goal is to calculate drift and deformation parameters in the area around the German research vessel Polarstern during its drift in the MOSAiC expedition.

To evaluate the retrieval, the algorithms are applied to SAR images (13 and 14 March 2020) for the area of the MOSAiC expedition. The result is promising for these SAR images. During this time interval, there was an opening event (in the overlap area of these two images). This event can be detected visually (by looking at and comparing the two SAR images). The algorithm result shows a high value of divergence at the location of the opening lead. It means according to the result, an observer should expect a possible opening in the next image. This expectation has consistency with the opening event that is observed visually.

The above-mentioned evaluation makes us confident to apply the algorithm for the area of our study, so for the whole Arctic winter, a large number of SAR images are selected carefully in the area of the MOSAiC expedition (two images per week with a high level of overlap). 3 deformation parameters (divergence, shear, and total deformation) and sea ice speed are calculated by the algorithm for whole pairs of images. Following that to investigate deformation and drift around Polastern, the mean values of all deformation parameters and also sea ice speed (Three square-shaped areas (with a square edge of 20, 60, and 100 km) in which the ship is located in the center of each square) are computed (for all pairs of image). This allows us to provide time-series of deformation parameters and mean speed around Polarstern.

In general, shear values are greater than the absolute values of divergence (here, one order of magnitude). In normal time (beyond anomalies), calculated mean values which are calculated for the larger area size are smaller (e.g., mean values for a square-shaped area with a square edge 100 km is smaller than the same one with a square edge 20 km) (ice drift in large scale follows a general pattern (e.g., transpolar drift), so mean values of deformation parameters are expected to be low). About ice mean speed, it variates a lot. The value of ice means speed is close to each other for different area sizes

except October (it could be because of comparatively low sea ice concentration at beginning of the freezing season).

In distinct anomalies, anomalies are more pronounced for a smaller area, but for less distinct anomalies it is vice versa (e.g., for the period between 19 Nov to 22 Nov in time-series, deformation values are higher for the square-shaped area with a square edge 20 km than the same one with square edge 100 km (it is vice versa for a normal time such as the period between 8 Nov and 12 Nov)). This may because of the location of the center of extreme events (e.g., an extreme event close to Polarstern produced distinct anomalies, so it is expected to have a higher value of mean deformation in a small area around the ship and while an extreme event happens far from Polarstern will produce less distinct anomalies, so less deformation in a small area around the ship in comparison is expected).

High value of deformation in early October may be explained by combination of a low ice thickness and concentration (e.g., at beginning of the expedition, it was hard to find an ice floe for RV Polarstern).

To have better interpretation, the time-series of mean value of meteorological data are illustrated in Fig 5.1. Fig 5.2 to Fig 5.6 also shows scatter plot our results with various meteorological data.

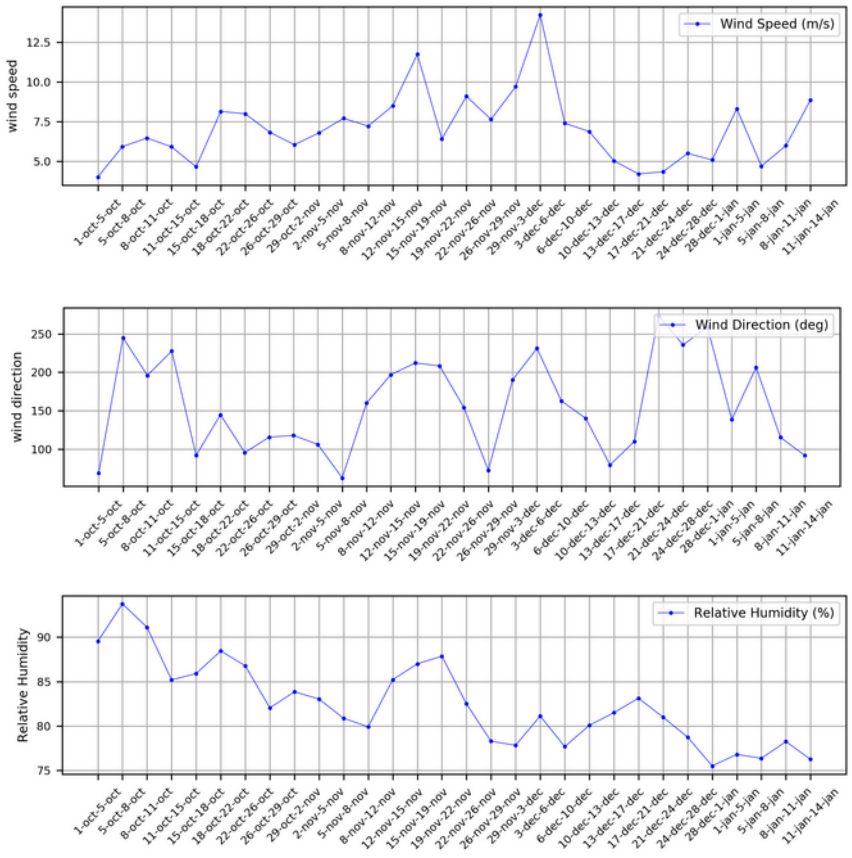

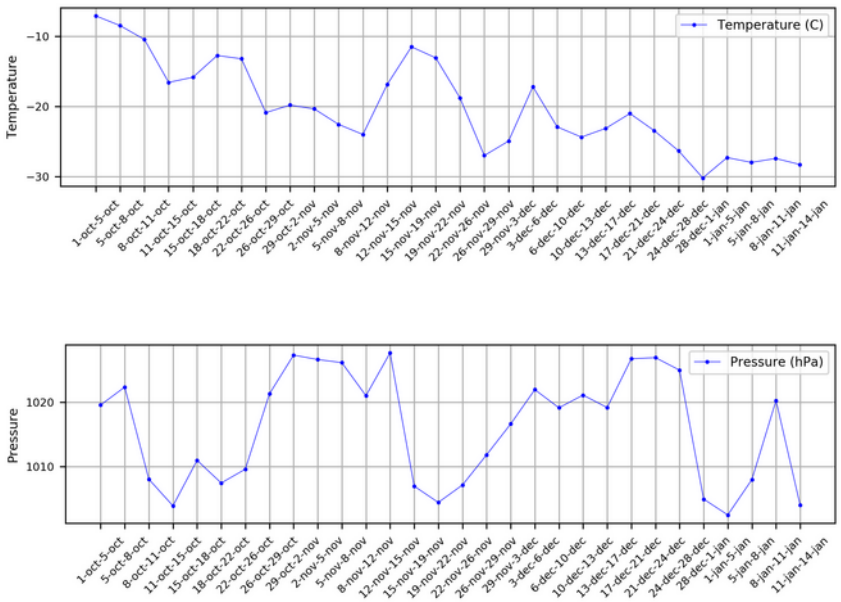

Fig 5.1 shows from up to down time-series of mean wind speed (m/s) , win direction (degree), mean relative humidity (%), mean temperature (ºC), and surface pressure (hPa) respectively (page 42 and 43).

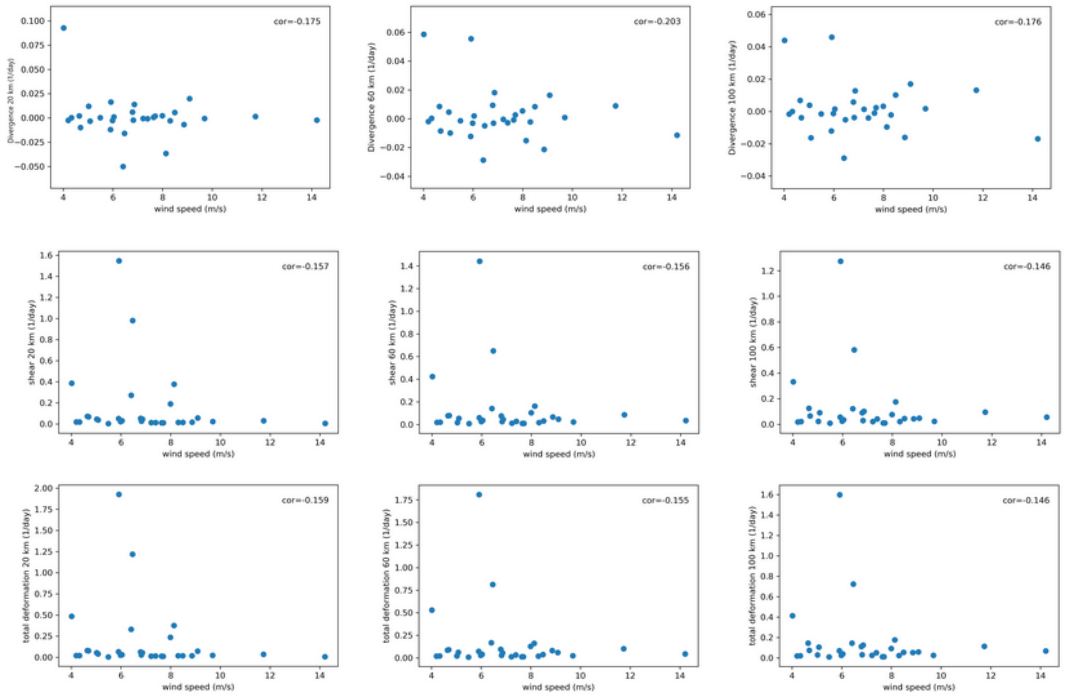

Fig 5.2 shows correlation plot of divergence with wind speed (first row), shear with wind speed (second row), and total deformation with wind speed (third row) (in each row from left to right mean values belong to area size with square edge 20, 60, and 100 km respectively (here all deformation value are in (1/day)).

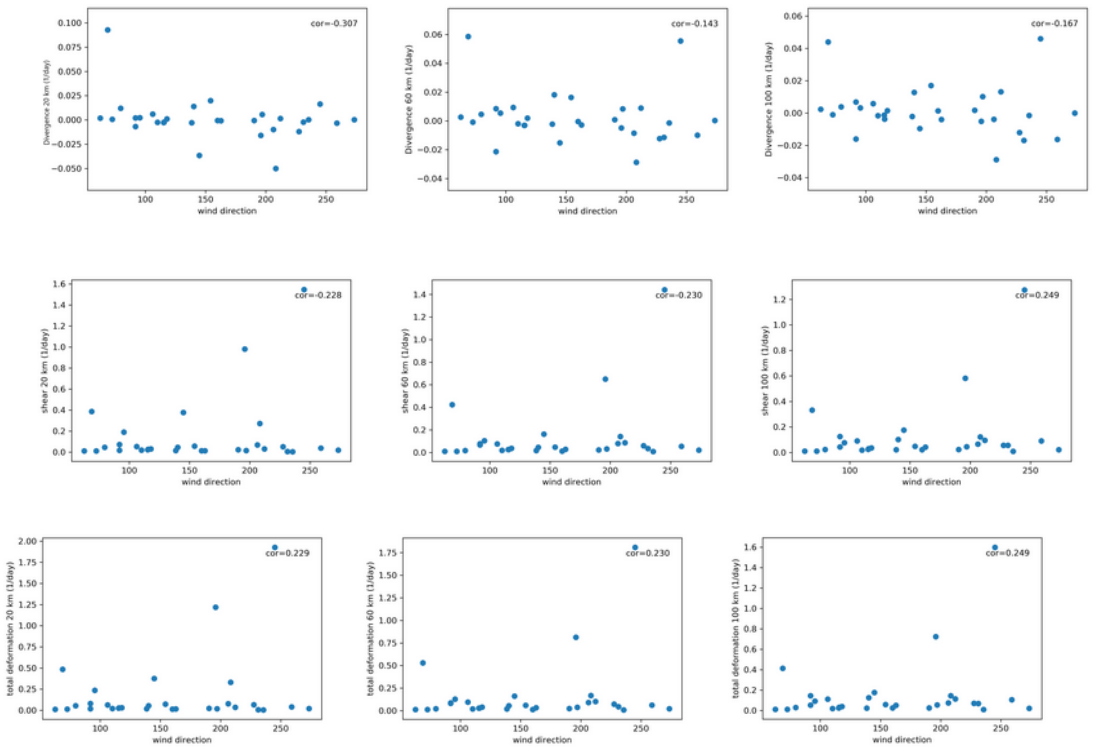

Fig 5.3 shows correlation plot of divergence with wind direction (first row), shear with wind direction (second row), and total deformation with wind direction (third row) (in each row from left to right mean values belong to area size with square edge 20, 60, and 100 km respectively (here all deformation value are in (1/day)).

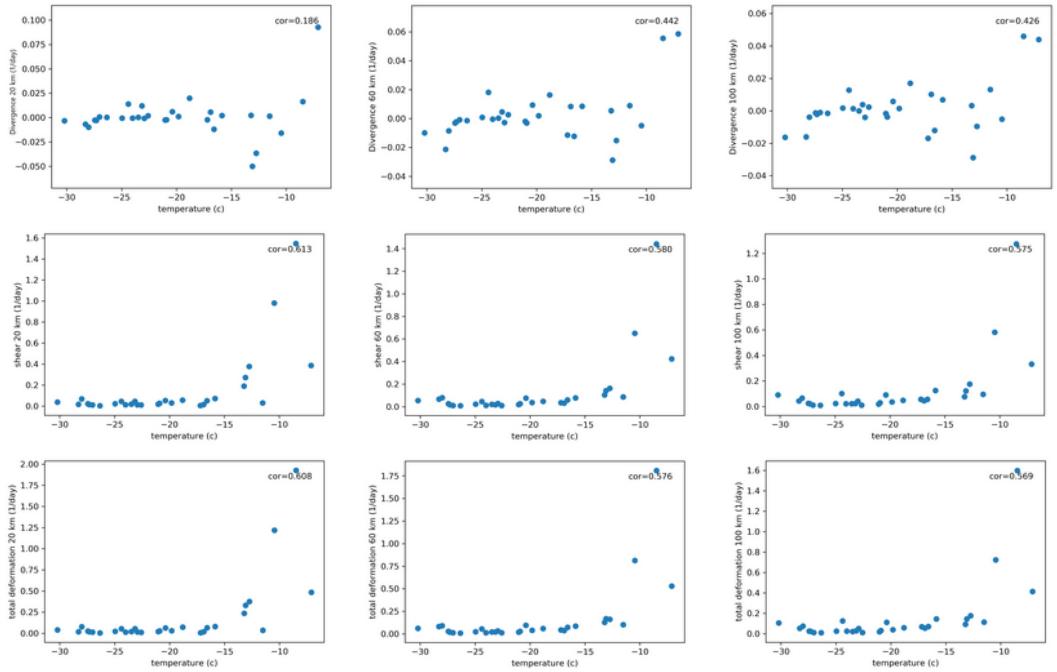

Fig 5.4 shows correlation plot of divergence with temperature (first row – page 44), shear with temperature (second row – page 44), and total deformation with temperature (third row) (in each row from left to right mean values belong to area size with square

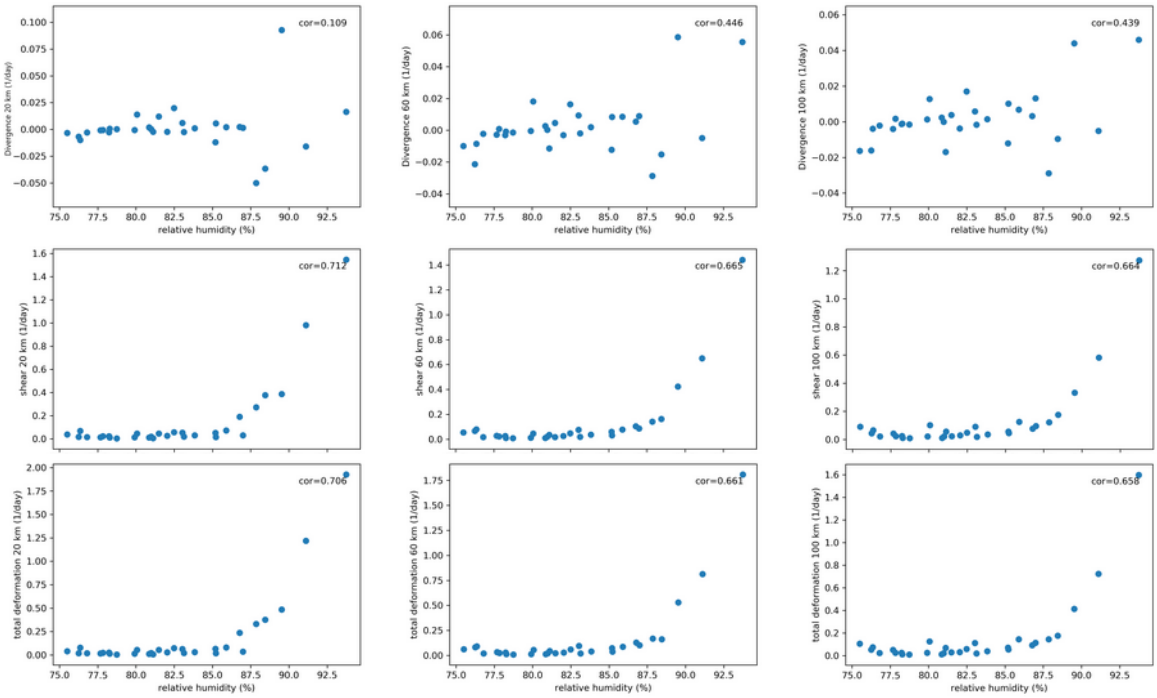

Fig 5.5 shows correlation plot of divergence with relative humidity (first row), shear with relative humidity (second row), and total deformation with relative humidity (third row) (in each row from left to right mean values belong to area size with square edge 20, 60, and 100 km respectively (here all deformation value are in (1/day)).

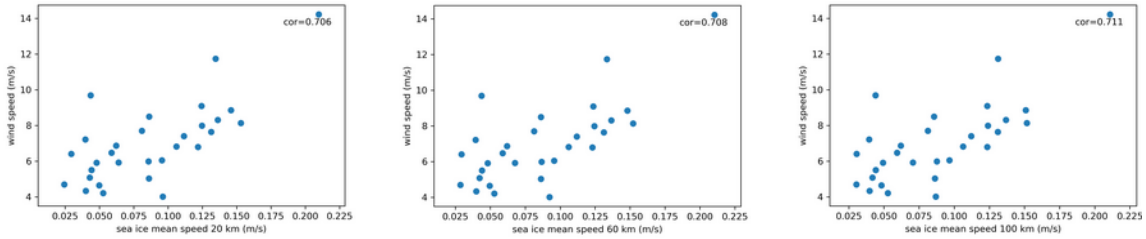

Fig 5.6

shows correlation plot of mean wind speed (m/s) with mean ice speed from left to right mean values belong to area size with square edge 20, 60, and 100 km respectively.

Correlation plots illustrate in general divergence, shear and total deformation do not correlate with wind speed and wind direction, but they correlate with temperature and relative humidity. Their correlation with relative humidity is stronger than their correlation with temperature. Shear and total deformation have a stronger correlation with temperature and relative humidity. The mean value of deformation parameters becomes less correlated with temperature and relative humidity when it calculates for a larger area (meteorological data of Polarstern would represent Polarstern location and

the area close more). The correlation plot which is demonstrated in Fig5.6 illustrates a good level of correlation between mean ice speed and wind speed (more detailed can be found in table 5.1).

Variable 1	Variable 2	Area (20 km)	Area (60 km)	Area (100 km)
Divergence	Wind speed	-0.175	-0.203	-0.176
Shear	Wind speed	-0.157	-0.156	-0.146
Total Deformation	Wind speed	-0.159	-0.155	-0.146
Divergence	Wind direction	-0.307	-0.143	-0.167
Shear	Wind direction	-0.228	-0.230	-0.249
Total Deformation	Wind direction	-0.229	-0.230	-0.249
Divergence	Temperature	0.186	0.442	0.426
Shear	Temperature	0.613	0.580	0.575
Total Deformation	Temperature	0.608	0.576	0.569
Divergence	Relative Humidity	0.109	0.446	0.439
Shear	Relative Humidity	0.712	0.665	0.664
Total Deformation	Relative Humidity	0.706	0.661	0.658
Wind speed	Ice speed	0.706	0.708	0.711

Table 5.1 shows all correlation value between ice kinematic variable and meteorological data from Polarstern.

By investigating in more depth and comparing deformation parameter time-series with time-series of meteorological data more correlation and interpretation will be revealed (these comparisons are shown in Fig 5.7 to Fig 5.12)

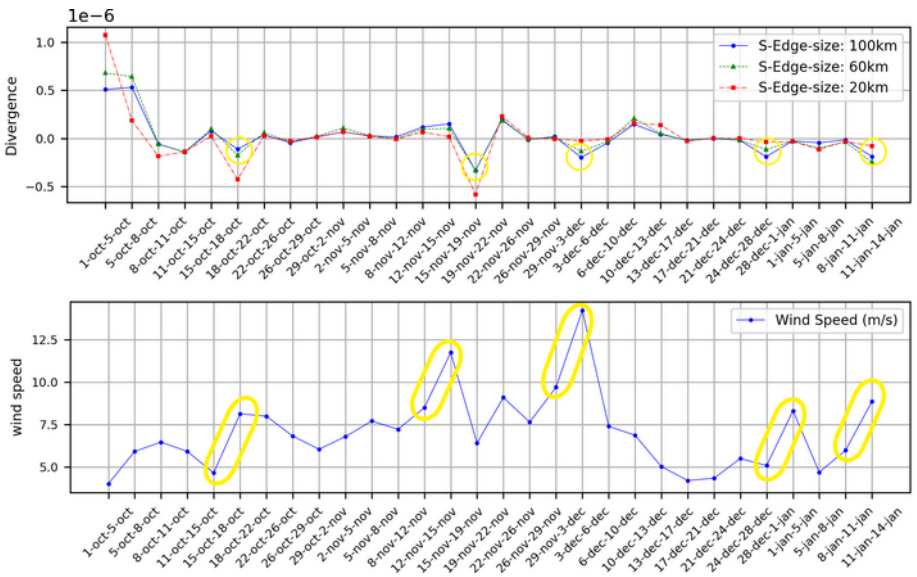

Fig 5.7 compares mean divergence time-series (1/s) with mean wind speed time-series (m/s) and shows correlation of rapid increase in wind speed

Fig 5.7 shows any rapid increase in wind speed will be followed by a convergence event (it is more pronounced in a larger area around Polarstern).

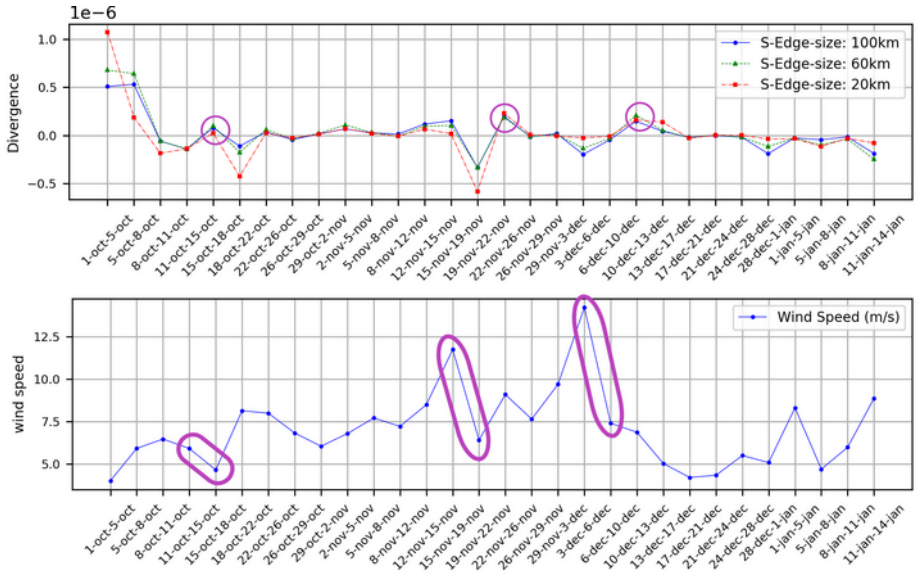

Fig 5.8 compares mean divergence time-series (1/s) with mean wind speed time-series (m/s) and shows correlation of rapid decrease in wind speed with divergence events.

Fig 5.8 shows any rapid decrease in wind speed will be followed by a divergence event (it is more pronounced in a larger area around Polarstern).

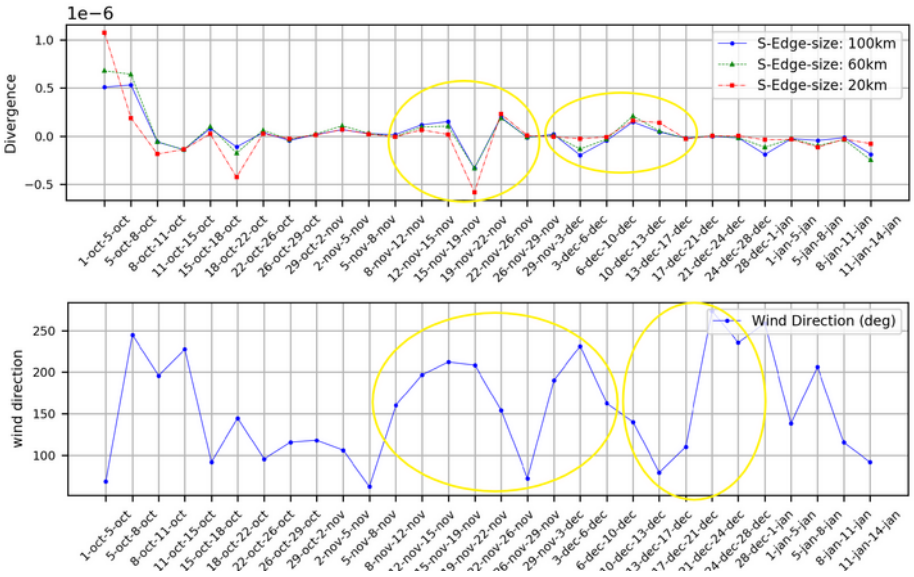

Fig 5.9 compares mean divergence time-series (1/s) with mean wind direction time-series (º) and shows correlation of rapid change in wind direction with divergence events.

Fig 5.9 illustrates that any rapid change in wind direction can be followed by a deformation event (divergence or convergence).

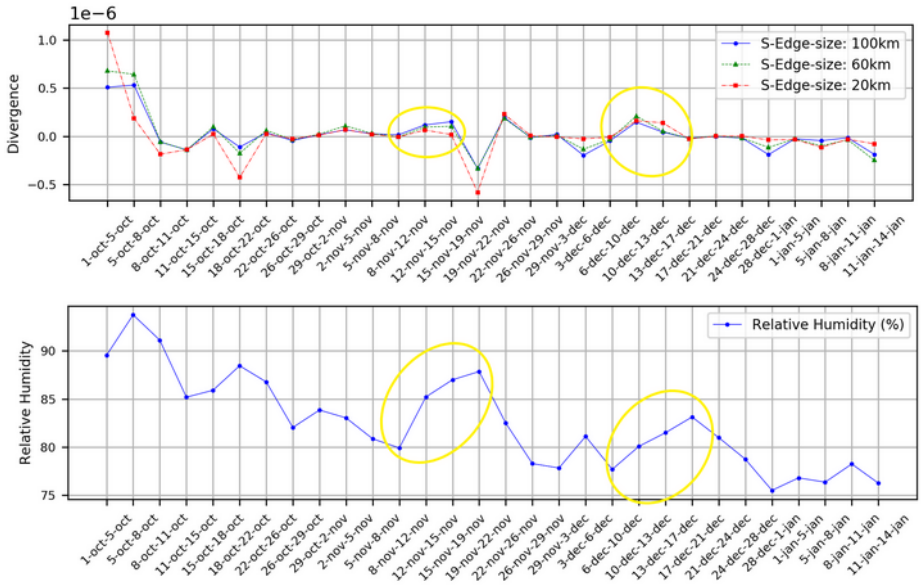

Fig 5.10 compares mean divergence time-series (1/s) with mean relative humidity time-series (%) and shows correlation of divergence events with rapid increase in relative humidity.

Fig 5.10 indicates that a long event of divergence can cause an increase in relative humidity. This can be explained by an increase in the lead fraction area which exposes the open ocean more to the atmosphere (which allows more moisture transport).

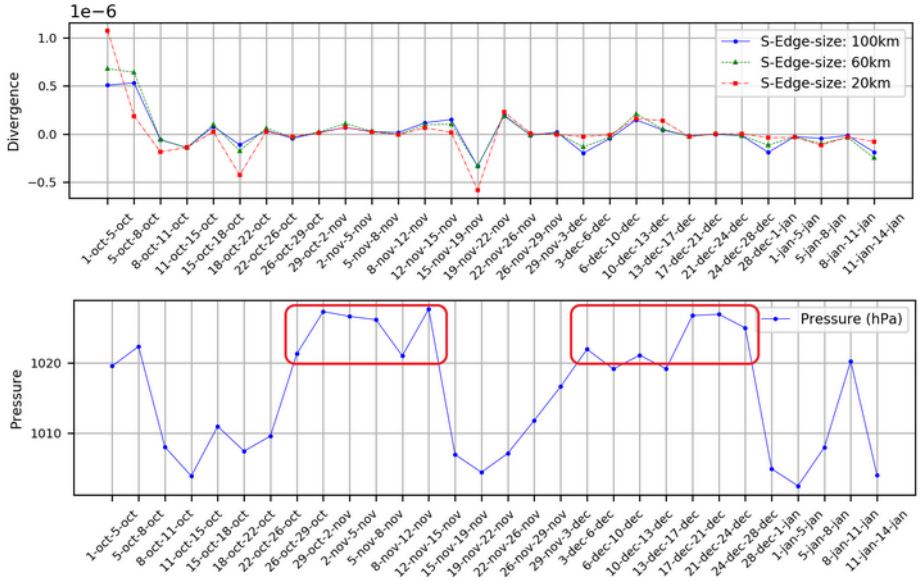

Fig 5.11 compares mean divergence time-series (1/s) with mean surface pressure time-series (hPa) and shows that in the period of high pressure we usually have low divergence.

High surface pressure usually means calm weather conditions. Fig 5.11 shows that there is no deformation event occurs during high surface pressure time (e.g., here above 1020 hPa).

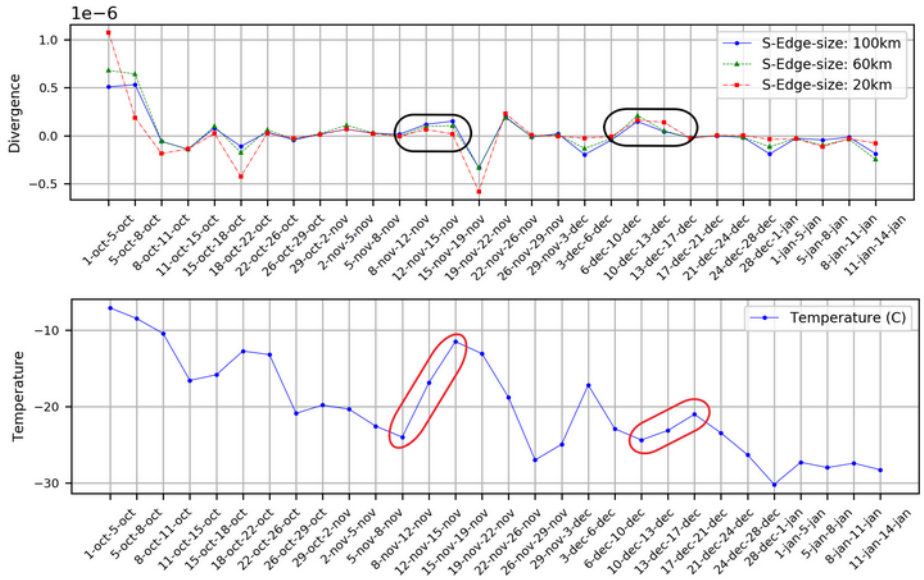

Fig 5.12 compares mean divergence time-series (1/s) with mean temperature time-series (º C) and shows correlation of divergence events with rapid increase in temperature.

Lead fraction has a large contribution to ocean-atmosphere heat fluxes. Fig 5.12 shows that there is a rise in temperature, happens during long period divergence event. This could be lead to an increase in lead fraction due to divergence event (as correlation not necessarily causation).

Our time-series do not cover the whole Arctic winter. It is generally because Sentinel 1 can cover the North pole and some area around (so when Polarstern was in this area we definitely have no deformation result at the location of Polarstern), but the lack of result is not only because that Sentinel 1 SAR data can cover the location of Polarstern. It is also because Sentinel 1 SAR data cannot cover fully all three square-shaped areas (which defined for deformation investigation) around Polastern (which means the result may not represent the area so they are discarded from further investigation) when Polarstern drifted toward the North pole. This lack of data gives us a room to work more for example, adaptation of our algorithm to other satellite SAR sensor such as TerraSAR-X.

Another room for improvement is moving from the Eulerian approach to Lagrangian, but why? A short answer is ice moves Lagrangian, but the extended answer comes as follow: A principal benefit of the Lagrangian movement representation is the capability to retrieve what is recognized as **L**inear **K**inematics **F**eatures (LKFs) and their temporal evolution (Kwok, 2003) (LKFs can be seen in Eulerian

approach, but not as well as Lagrangian approach). Almost all deformation shapes of the ice cover are localized throughout these linear features (Shokr and N Sinha 2015). Except for (Herman and Glowacki, 2012), who used gridded Eulerian data in a spatial scaling analysis, scaling analyses of sea ice deformation are established on Lagrangian trajectories, either comes from satellite data (Marsan et al., 2004; Stern & Lindsay, 2009), taped by buoys (Rampal et al., 2008; Hutchings et al., 2011, 2012), or modeled in a Lagrangian core (Rampal et al., 2016). The two Lagrangian and Eulerian ways ought to, in theory, direct to the identical spatial scaling output (if small time scales are considered where the advection of ice between two time-steps is negligible), but the temporal scaling characteristic relied upon the deformation history of individual ice floes. Eulerian averaging over a fixed box in space fails to consider the advection of this deformation history so that this memory impact can only be taken into account by following one parcel of ice throughout time. For that reason, the temporal scaling analysis needs a Lagrangian framework. Nevertheless, the calculation of strain rates from Lagrangian trajectories is known to produce errors by the picking of cell borderlines and the discontinuities in the ice movement (Lindsay & Stern, 2003). These errors cause an overestimation of the scaling exponents (Bouillon & Rampal, 2015a). Because sea ice is a brittle solid, it does not deform together with the all ice cover; rather, sea ice drifts and deforms because of fractures/cracks are produced by brittle failure. As local ice strength is dictated by weaknesses in the fracture structures that advect with the ice cover, the Lagrangian method is more suitable, where details of ice kinematics and the openings and closings of the ice cover, for understanding ice mechanics and surface heat balance is of interest (Kwok, 2010).

To advance our drift result we can take the benefits of dual-polarization. Now, we exploit HV polarization because of its better performance. We can use feature-tracking on both polarization modes and combine them to produce an enhanced first estimation. Then we can use this dual-polarized data individually in the pattern matching phases. So the result could be compared and finally merged into one.

We can combine our result with classification from SAR images to produce high-resolution ice maps which is helpful for many other researchers like sea-ice modelers, sea-ice forecaster, and climate researchers.

During the MOSAiC expedition, relatively large buoys record their locations in relatively short intervals. These locations help to calculate the in-situ deformation parameter. these values can be compared with the retrieved value from the satellite in a future job.

6| References

Aagaard, K., L. Coachman, and E. Carmack (1981), On the halocline of the arctic ocean, Deep Sea Res., Part A, 28(6), 529– 545.

Andreas, E. and Murphy, B.: Bulk transfer coefficients for heat and momentum over leads and polynyas, J. Phys. Oceanogr., 16, 1875–1883, 1986.

Arya, S. P. S. 1973. Contribution of form drag on pressure ridges to the air stress on Arctic ice. Journal of Geophysical Research (1896-1977), 78(30), 7092–7099.

Asplin, M. G., Galley, R., Barber, D. G., & Prinsenberg, S. 2012. Fracture of summer perennial sea ice by ocean swell as a result of Arctic storms. Journal of Geophysical Research: Oceans, 117(C6), 1–12. C06025

Barton, I.J. Ocean Currents from Successive Satellite Images: The Reciprocal Filtering Technique. J. Atmos. Ocean. Technol. 2002, 19, 1677–1689

Bird, K. J., Charpentier, R. R., Gautier, D. L., Houseknecht, D. W., Klett, T. R., Pitman, J. K., Moore, T. E., Schenk, C. J., Tennyson, M. E., & Wandrey, C. J. 2008. Circum-Arctic Resource Appraisal: Estimates of Undiscovered Oil and Gas North of the Arctic Circle

Bouillon, S., & Rampal, P. 2015a. On producing sea ice deformation data sets from SAR-derived sea ice motion. The Cryosphere, 9(2), 663–673.

Calonder M. , V. Lepetit, C. Strecha, and P. Fua. Brief: Binary robust independent elementary features. In In European Conference on Computer Vision, 2010.

Carrieres, T., Buehner, M., Lemieux, J., & Toudal Pedersen, L. (Eds.). (2017). Sea Ice Analysis and Forecasting: Towards an Increased Reliance on Automated Prediction Systems. Cambridge: Cambridge University Press. Doi:10.1017/9781108277600

Collins, Michael J. and William J. Emery 1988 'A Computational Method for Estimating Sea Ice Motion in Sequential Seasat Synthetic Aperture Radar Imagery by Matched Filtering', Journal of Geophysical Research, 93, C8, pp. 9241–9251, doi:10.1029/JC093iC08p09241.

Cox, G., & Weeks, W. (1974). Salinity Variations in Sea Ice. Journal of Glaciology, 13(67), 109-120. doi:10.3189/S0022143000023418

Daida J., R. Samadani, and J. F. Vesecky, "Object-oriented Feature-tracking algorithms For SAR image of the marginal ice zone," IEEE Trans. Geosci. Remote Sens., vol. 28, no. 4, pp. 573–589, Jul. 1990.

Dierking, W. 2013. Sea ice monitoring by synthetic aperture radar. Oceanography 26(2):100–111, https://doi.org/10.5670/oceanog.2013.33.

Drinkwater M. R. , Satellite Microwave Radar Observations of Antarctic Sea Ice. Germany, Berlin:Springer-Verlag, 1998, pp. 145–187.

Egu´ıluz, V. M., Fernandez-Gracia, J., Irigoien, X., & Duarte, ´ C. M. 2016. A quantitative assessment of Arctic shipping in 2010 – 2014. Scientific Reports, 6(30682)

ESA: Sentinel-1 ESA's Radar Observatory Mission for GMES Operational Services, ESA Communications, SP-1322/1, ESA, the Netherlands, 2012.

ESA (European Space Agency). Copernicus Sentinels Scientific Data Hub. 2014. Available online: https://scihub.copernicus.eu/ (accessed on 3 July 2020)

Fily M. and D. A. Rothrock, "Sea ice tracking by nested correlations,"IEEE Trans. Geosci. Remote Sens., vol. 25, no. 5, pp. 570–580, Sep. 1987.

Fily, M., and Rothrock, D. A. (1990), Opening and closing of sea ice leads: Digital measurements from synthetic aperture radar, J. Geophys. Res., 95(C1), 789– 796, doi:10.1029/JC095iC01p00789.

Farrell, S. L., S. W. Laxon, D. C. McAdoo, D. Yi, and H. J. Zwally (2009), Five years of Arctic sea ice freeboard measurements from the Ice, Cloud and land Elevation Satellite, J. Geophys. Res., 114, C04008, doi:10.10 29/2008jc005074

Geiger, Cathleen A., William D. Hibler III and Stephen F. Ackley 1998 'Large-scale sea ice drift and deformation: Comparison between models and observations in the western Weddell Sea during 1992', Journal of Geophysical Research, 103, C10 [Sept. 1998], pp. 21893– 21913, doi: 10.1029/98JC01258.

Giles A. B. , R. A. Massom, P. Heil, and G. Hyland, "Semi-automated feature-tracking of East Antarctic sea ice from Envisat ASAR imagery," Remote Sens. Environ., vol. 115, no. 9, pp. 2267–2276, 2011.

Girard, L., Weiss, J., Molines, J.-M., Barnier, B., and Bouillon, S.: Evaluation of high-resolution sea ice models on the basis of statistical and scaling properties of Arctic sea ice drift and deformation, J. Geophys. Res., 114, 2156–2202, 2009.

Girard, L., Bouillon, S., Weiss, J., Amitrano, D., Fichefet, T., and Legat, V.: A new modelling framework for sea ice mechanics based on elasto-brittle rheology, Ann. Glaciol., 52, 123–132, 2011.

Gultepe I., Zhou B., Milbrandt J., Bott A., Li Y., Heymsfield A.J., Ferrier B., Ware R., Pavolonis M., Kuhn T., Gurka J., Liu P., Cermak j., "A review on ice fog measurements and modeling," Atmos. Res., vol. 151, pp. 2–19, Jan. 2015.

Hader, M., 1996 ‘Dynamik, Rauhigkeit und Alter des Meereises in der Arktis - Numerische Untersuchungen in einem großskaligen Modell’, Berichte zur Polarforschung, 1996, 203, ed. by Franz Riemann, issn: 0176-5027, http://hdl.handle.net/10013/epic.10204.d001.

Hall, R.T. and D.A. Rothrock 1981 ‘Sea Ice Displacement From Seasat Synthetic Aperture Radar’, Journal of Geophysical Research, 86, C11, pp. 11078–11082, doi: 10.1029/JC086iC11p11078.

Hall, C. M., & Saarinen, J. 2010. Polar Tourism: Defnitions and Dimensions. Scandinavian Journal of Hospitality and Tourism, 10(4), 448–467.

Hansen, M. W. ; Kloster, K. ; Dagestad, K. ; Sandven, S. ; Johannessen, J. A. 2010 ‘Retrieval of Sea Ice Drift from SAR Doppler Shift’,

Herman, A., & Glowacki, O. 2012. Variability of sea ice deformation rates in the Arctic and their relationship with basin-scale wind forcing. The Cryosphere, 6(6), 1553–1559

Hollands, T., and Dierking W., 2011 ‘Performance of a multiscale correlation algorithm for the estimation of sea ice drift from SAR images: initial results’, Annals of Glaciology, 52, 57 [May 2011], pp. 311–317, doi: 10.3189/172756411795931462.

Holloway, G., & Proshutinsky, A. 2007. Role of tides in Arctic ocean/ice climate. Journal of Geophysical Research: Oceans, 112(C4), 1–10. C04S06.

Horvat, C., Tziperman, E., & Campin, J.-M. 2016. Interaction of sea ice foe size, ocean eddies, and sea ice melting. Geophysical Research Letters, 43(15), 8083–8090.

Hutchings, J. K., Roberts, A., Geiger, C., & Richter-Menge, J. 2011. Spatial and temporal characterization of sea-ice deformation. Annals of Glaciology, 52(57), 360–368.

Itkin, P., Spreen, G., Hvidegaard, S. M., Skourup, H., Wilkinson, J., Gerland, S., et al. (2018). Contribution of deformation to sea ice mass balance: A case study from an N-ICE2015 storm. Geophysical Research Letters, 45, 789–796. https://doi.org/10.1002/2017GL076056

Iacozza, J., & Barber, D. G. 1999. An examination of the distribution of snow on seaice. Atmosphere-Ocean, 37(1), 21–51

Karvonen J. , “Operational SAR-based sea ice drift monitoring over the Baltic Sea,” Ocean Sci., vol. 8, no. 4, p. 473, 2012.

Koerner RM (1973) The mass balance of sea ice of the Arctic Ocean. J Glaciol 12, no 65: 173–185

Komarov A. S. and D. G. Barber, “Sea ice motion tracking from sequential dual-polarization RADARSAT-2 images,” IEEE Trans. Geosci. Remote Sens., vol. 52, no. 1, pp. 121–136, Jan. 2014.

Korosov, A.; Hansen, M.W.; Yamakawa, A.; Dagestad, K.F.; Vines, A.; Riechert, M.; Myasoedov, A.; Morozov, E.; Piotrovskaya, N.; Williams, T. Nansat-0.6.14, 2016. Available online: https://doi.org/10.5281/zenodo.59998 (accessed on 3 November 2017).

Korosov, A.A.; Rampal, P. A Combination of Feature Tracking and Pattern Matching with Optimal Parametrization for Sea Ice Drift Retrieval from SAR Data. Remote Sens. 2017, 9, 258.

Kræmer, T. ; Johnsen, H. ;Brekke, C ;Engen, G. ‘Comparing SAR-Based Short Time-Lag Cross Correlation and Doppler-Derived Sea Ice Drift Velocities’ IEEE Transactions on Geoscience and Remote Sensing (Volume: 56 , Issue: 4 , April 2018).

Kwok R. , J. C. Curlander, R. McConnell, and S. S. Pang, “An ice-motion tracking system at the Alaska SAR facility,” IEEE J. Ocean. Eng., vol. 15, no. 1, pp. 44–54, Jan. 1990.

Kwok R. , A. Schweiger, D. A. Rothrock, S. Pang, and C. Kottmeier, “Sea ice motion from satellite passive microwave imagery assessed with ERS SAR and buoy motions,” J. Geophys. Res., Oceans, vol. 103, no. C4, pp. 8191–8214, 1998.

Kwok, R. 2001. Deformation of the Arctic Ocean Sea Ice Cover between November 1996 and April 1997: A Qualitative Survey. Pages 315–322 of: Dempsey, J., & Shen, H. (eds), IUTAM Symposium on Scaling Laws in Ice Mechanics and Ice Dynamics. Solid Mechanics and Its Applications, vol. 94. Springer Netherlands.

Kwok, R. 2006. Contrasts in sea ice deformation and production in the Arctic seasonal and perennial ice zones. Journal of Geophysical Research: Oceans, 111(C11). C11S22.

Kwok, R., Hunke, E. C., Maslowski, W., Menemenlis, D., & Zhang, J. 2008. Variability of sea ice simulations assessed with RGPS kinematics. Journal of Geophysical Research: Oceans, 113(C11), 1–20. C11012.

Kwok, R., and G. F. Cunningham (2008), ICESat over Arctic sea ice: Estimation of snow depth and ice thickness, J. Geophys. Res., 113, C08010, doi:10.1029/2008JC004753.

Kwok, R., G. Spreen, and S. Pang (2013), Arctic sea ice circulation and drift speed: Decadal trends and ocean currents, J. Geophys. Res. Oceans, 118, 2408–2425, doi:10.1002/jgrc.20191

Kwok, R., & Cunningham, G. (2015). Variability of Arctic sea ice thickness and volume from CryoSat-2. Philosophical Transactions of the Royal Society A: Mathematical, Physical and Engineering Sciences, 373, 20140157. https://doi.org/10.1098/rsta.2014.0157

Lemieux, J.-F., Tremblay, L. B., Dupont, F., Plante, M., Smith, G. C., & Dumont, D. 2015. A basal stress parameterization for modeling landfast ice. Journal of Geophysical Research: Oceans, 120(4), 3157–3173.

Leppäranta, M. (2005), The Drift of Sea Ice, 266 pp., Springer, Heidelberg, Germany. Lewis, J. P. 1995 'Fast Normalized Cross-Correlation', in Proceedings of Vision Interface 95, Quebec City, Canada, pp. 120–123.

Lindsay, R. W., & Rothrock, D. A. 1995. Arctic sea ice leads from advanced very high resolution radiometer images. Journal of Geophysical Research: Oceans, 100(C3), 4533–4544.

Lindsay, R. W. and Stern, H. L.: The RADARSAT Geophysical Processor System: Quality of Sea Ice Trajectory and Deformation Estimates, J. Atmos. Ocean. Tech., 20, 1333–1347, https://doi.org/10.1175/1520-0426(2003)020<1333:TRGPSQ>2.0.CO;2, 2003.

Lindsay R. W., Zhang J.,Rothrock A., (2003) Sea-ice deformation rates from satellite measurements and in a model, Atmosphere-Ocean, 41:1, 35-47, DOI: 10.3137/ao.410103

Liu A. K. , S. Martin, and R. Kwok, "Tracking of ice edges and ice floes by wavelet analysis of SAR images," J. Atmos. Ocean. Technol., vol. 14, no. 5, pp. 1187–1198, 1997.

Lüpkes, C., V. M. Gryanik, B. Witha, M. Gryschka, S. Raasch and T. Gollnik 2008 'Modeling convection over arctic leads with LES and a non-eddyresolving microscale model', Journal of Geophysical Research, 113, C09028 [Sept. 2008], p. 17, doi: 10.1029/2007JC004099.

Maher, P. T. 2017. Tourism Futures in the Arctic. Cham: Springer International Publishing. Pages 213–220.

Mahoney, A., Eicken, H., & Shapiro, L. 2007. How fast is landfast sea ice? A study of the attachment and detachment of nearshore ice at Barrow, Alaska. Cold Regions Science and Technology, 47(3), 233 – 255.

MANICE (2005), Manual of Standard Procedures for Observing and Reporting Ice Conditions, Catalo. No. EN56–175/2005, Can. Ice Service — Environ. Can., Ottawa, Ontario, Canada.

Marcq, S., and J. Weiss (2012), Influence of sea ice lead -width distribution on turbulent heat transfer between the ocean and the atmosphere, The Cryosphere, 6, 143–156, doi:10.5194/tc-6-143-2012.

Marko, J. R., & Thomson, R. E. 1977. Rectilinear leads and internal motions in the ice pack of the Western Arctic Ocean. Journal of Geophysical Research, 82(6), 979–987.

Marsan, D., Stern, H., Lindsay, R., & Weiss, J. 2004. Scale Dependence and Localization of the Deformation of Arctic Sea Ice. Phys. Rev. Lett., 93(Oct), 178501.

Maykut GA (1982) Large scale heat exchange and ice production in the Central Arctic. J Geophys Res 87, no C10:7971–7984

Maykut, G. A. (1986), The surface heat and mass balance, Geophysics of Sea Ice. NATO Adva. Sci. Inst. Ser. B (Physics), vol. 146, edited by N. Untersteiner, pp. 395–463, Plenum Press, New York.

McConnell R. , R. Kwok, J. C. Curlander, W. Kober, and S. S. Pang, "ψ-s correlation and dynamic time warping: Two methods for tracking ice floes in SAR images," IEEE Trans. Geosci. Remote Sens., vol. 29, no. 6, pp. 1004–1012, Nov. 1991.

McLaren, A. J., H. T. Banks, C. F. Durman, J. M. Gregory, T. C. Johns, A. B. Keen, J. K. Ridley, M. J. Roberts, W. H. Lipscomb, W. M. Connolley and S . W. Laxon 2006 'Evaluation of the sea ice simulation in a new coupled atmosphereocean climate model (HadGEM1)', Journal of Geophysical Research, 111, C12014 [Dec. 2006], pp. 1–17, doi: 10.1029/2005JC003033.

McPhee, M. G., R. Kwok, R. Robins, and M. Coon (2005), Upwelling of arctic pycnocline associated with shear motion of sea ice, Geophys. Res. Lett., 32(10), doi:10.1029/2004GL021819.

A. Moreira, P. Prats-Iraola, M. Younis, G. Krieger, I. Hajnsek, and K. P. Papathanassiou, "A tutorial on synthetic aperture radar," IEEE Geosci. Remote Sens. Mag., vol. 1, no. 1, pp. 6–43, Mar. 2013.

Morison JH, McPhee MG, Curtin TB, Paulson CA (1992) The oceanography of winter leads. J Geophys Res 97, no C7:11199–11218

Muckenhuber S., A. A. Korosov, and S. Sandven, "Open-source feature-tracking algorithm for sea ice drift retrieval from Sentinel-1 SAR imagery," Cryosphere, vol. 10, no. 2, pp. 913–925, 2016.

Muckenhuber, S. and Sandven, S.: Open-source sea ice drift algorithm for Sentinel-1 SAR imagery using a combination of feature tracking and pattern matching, The Cryosphere, 11, 1835–1850, https://doi.org/10.5194/tc-11-1835-2017, 2017.

Nansen, Fridtjof 1902 The Oceanography of the North Polar Basin. Scientific Results, vol. 3, 9, Longman Green & Co., Kristinania, Norway

Nguyen, A. T., Kwok, R., & Menemenlis, D. 2012. Source and Pathway of the Western Arctic Upper Halocline in a Data-Constrained Coupled Ocean and Sea Ice Model. Journal of Physical Oceanography, 42(5), 802–823.

Nomura, D., Aoki, S., Simizu, D., & Iida, T. 2018. Influence of Sea Ice Crack Formation on the Spatial Distribution of Nutrients and Microalgae in Flooded Antarctic Multiyear Ice. Journal of Geophysical Research: Oceans, 123(2), 939–951.

Overland, J. E., & Wang, M. 2013. When will the summer Arctic be nearly sea ice free? Geophysical Research Letters, 40(10), 2097–2101.

Onana, V., N. T. Kurtz, S. L. Farrell, L. S. Koenig, M. Studinger, and J. P. Harbeck (2013), A sea-ice lead detection algorithm for use with high-resolution airborne visible imagery, IEEE Trans. Geosci. Remote Sens., 51(1), 38–56.

Pärn, O. and J. Haapala (2011), Occurence of synoptic flaw leads of sea ice in the Gulf of Finland, Boreal Environ. Res., 16, 71–78.

Rampal, P., Weiss, J., & Marsan, D. 2009. Positive trend in the mean speed and deformation rate of Arctic sea ice, 19792007. Journal of Geophysical Research: Oceans, 114(C5)

Rampal, P., Bouillon, S., Ólason, E., and Morlighem, M.: neXtSIM: a new Lagrangian sea ice model, The Cryosphere, 10, 1055–1073, https://doi.org/10.5194/tc-10-1055-2016, 2016.

Richter-Menge, J. A., McNutt, S. L., Overland, J. E., & Kwok, R. 2002. Relating Arctic pack ice stress and deformation under winter conditions. Journal of Geophysical Research: Oceans, 107(C10), SHE 15–1–SHE 15–13.

Rosin P. L., Measuring corner properties. Computer Vision and Image Understanding, 73(2):291 - 307, 1999.

Rosten, E. and Drummond, T.: Machine learning for highspeed corner detection, in: European Conference on Computer Vision, 7–13 May 2006, Graz, Austria, 430–443, https://doi.org/10.1007/11744023_34, 2006.

Rothrock, D. A., & Thorndike, A. S. 1984. Measuring the sea ice foe size distribution. Journal of Geophysical Research: Oceans, 89(C4), 6477–6486.

Rublee, E., Rabaud, V., Konolige, K., and Bradski, G.: ORB: an efficient alternative to SIFT or SURF, IEEE I. Conf. Comp. Vis. (ICCV), 6–13 November 2011, Barcelona, Spain, 2564–2571, https://doi.org/10.1109/ICCV.2011.6126544, 2011.

Ruffieux, D., et al. (1995), Ice pack and lead surface energy budgets during LEADEX 1992, J. Geophys. Res., 100 (C3), 4593–4612.

Schulson, E. M., & Hibler, W. D. 1991. The fracture of ice on scales large and small: Arctic leads and wing cracks. Journal of Glaciology, 37(127), 319–322.

Shokr, M., and Sinha, N., (2015), Sea Ice: Physics and Remote Sensing, 600 pp., Wiley, USA

Smith, L. C., & Stephenson, S. R. 2013. New Trans-Arctic shipping routes navigable by midcentury. Proceedings of the National Academy of Sciences, 110(13), E1191–E1195.

Spreen, G., R. Kwok, and D. Menemenlis (2011), Trends in Arctic sea ice drift and role of wind forcing: 1992–2009, Geophys. Res. Lett., 38, L19501, doi:10.1029/2011GL048970.

Spreen, G., Kwok, R., Menemenlis, D., & Nguyen, A. T. 2016. Sea Ice Deformation in a Coupled Ocean-Sea Ice Model and in Satellite Remote Sensing Data. The Cryosphere Discussions, 2016, 1–37.

Squire, V. A., Dugan, J. P., Wadhams, P., Rottier, P. J., & Liu, A. K. 1995. Of Ocean Waves and Sea Ice. Annual Review of Fluid Mechanics, 27(1), 115–168.

Stern, H. L., & Lindsay, R. W. 2009. Spatial scaling of Arctic sea ice deformation. Journal of Geophysical Research: Oceans, 114(C10), n/a–n/a. C10017.

Stroeve, J. C., Kattsov, V., Barrett, A., Serreze, M., Pavlova, T., Holland, M., & Meier, W. N. 2012. Trends in Arctic sea ice extent from CMIP5, CMIP3 and observations. Geophysical Research Letters, 39(16).

Sun Y. , "Automatic ice motion retrieval from ERS-1 SAR images using the optical flow method," Int. J. Remote Sens., vol. 17, no. 11, pp. 2059–2087, 1996.

Thomas, M., Geiger, C. A., and Kambhamettu, C.: High resolution (400 m) motion characterization of sea ice using ERS-1 SAR imagery, Cold Reg. Sci. Technol., 52, 207–223, 2008

Thorndike, A. S., Rothrock, D. A., Maykut, G. A., & Colony, R. 1975. The thickness distribution of sea ice. Journal of Geophysical Research (1896-1977), 80(33), 4501–4513.

Thorndike, A. S., and R. Colony (1982), Sea ice motion in response to geostrophic winds, J. Geophys. Res., 87(C8), 5845–5852.

Tremblay, L.B., M.M. Holland, I.V. Gorodetskaya, and G.A. Schmidt, 2007: An ice-free Arctic? Opportunities for computational science. Comput. Sci. Eng., 9, no. 3, 65-74.

Tsamados, M., Feltham, D. L., Schroeder, D., Flocco, D., Farrell, S. L., Kurtz, N., Laxon, S. W., & Bacon, S. 2014. Impact of Variable Atmospheric and Oceanic Form Drag on Simulations of Arctic Sea Ice. Journal of Physical Oceanography, 44(5), 1329–1353.

Vesecky, R. Samadani, M. P. Smith, J. M. Daida, and R. N. Bracewell, "Observation of sea-ice dynamics using synthetic aperture radar images: Automated analysis," IEEE Trans. Geosci. Remote Sens., vol. 26, no. 1, pp. 38–48, Jan. 1988.

Vaughan, D.G.; Comiso, J.C.; Allison, I.; Carrasco, J.; Kaser, G.; Kwok, R.; Mote, P.; Murray, T.; Paul, F.; Ren, J.; et al. Observations: Cryosphere. In Climate Change 2013: The Physical Science Basis. Contribution of Working Group I to the Fifth Assessment Report of the Intergovernmental Panel on Climate Change; Stocker, T., Qin, D., Plattner, G., Tignor, M., Allen, S., Boschung, J., Nauels, A., Xia, Y, Bex, V., Midgley, P.M., Eds.; Cambridge University Press: Cambridge, UK, 2013; pp. 317–382.

Yang J, Neelin JD (1993) Sea-ice interaction with the thermohalinecirculation. Geophys Res Lett 20:217–220

Appendix A: Pattern-matching

In a given sequence of image, if an algorithm searches a template (a relative very small piece of image (a patch)) from the first image in the entire (or the most probable) area of the search image (the second image) to find the exact (or the best) match, it considers as a pattern-matching algorithm.

In contrast, a feature-tracking algorithm detects features in the both images first and matches features between the first image and the second image as second step.

Template-based matching approach generally describes by using Sum of Absolute Differences (SAD) or cross-correlation. Both will explain as follow respectively:

The sum of absolute differences (SAD) here is measure of the similarity between the value of template itself (as patch of the first image) and its corresponding in the search image (the second image). It is calculated by taking the summation of the absolute differences between each pixel original value of the template (value of that pixel in the first image) and its correspond value in the second image. It can be formulated by:

$$\mathrm{SAD}(u,v)=\sum_{i=0}^{g\,row}\sum_{j=0}^{g\,column}\left|h_{(u,v)}(x_i,y_j)-g(x_i,y_j)\right| \qquad \text{(A-1)}$$

"(u, v)" is the coordinate on the search image (which calculation applies on it). "g" is the template with its original in the first image. "$h_{(u,v)}$" is the value of the template which center of template is located on (u,v) in the second image.

The final result of this method is a matrix of SADs with the size slightly smaller than the size of search image (exact size is dominated by the size of template). The location of the smallest value of the matrix represents the location of the best match in the second image.

As an example, if we have template and the search image which each pixel of them is defined by a single integer from 0 to 9 as follow:

Template	Search image
2 5 5	2 7 5 8 6
4 0 7	1 7 4 2 7
7 5 9	8 4 6 8 5

Then absolute differences are calculated for blue, red and yellow as follow:

Blue	Red	Yellow
0 2 0	5 0 3	3 3 1
3 7 3	3 4 5	0 2 0
1 1 3	3 1 1	1 3 4

So for our example, the matrix of SAD is [20, 25, 17] this means best match is located in yellow in the second image.

The other method for template-based matching approach is the cross-correlation. The motivation of the concept of the cross-correlation comes from the distance measurement (squared Euclidean distance). Sum of Squared Distance (SSD) is formulated as below:

$$\mathrm{SSD}(u,v)=\sum_{i=0}^{g\,row}\sum_{j=0}^{g\,column}\left[h_{|u,v|}(x_i,y_j)-g(x_i,y_j)\right]^2 \qquad \text{(A-2)}$$

Parameters have a similar definition like SAD and SSD(u,v) is SSD in position (u,v) in the second image. Expansion of the SSD formula leads to:

$$\mathrm{SSD}(u,v)=\sum_{i=0}^{g\,row}\sum_{j=0}^{g\,column}\left[h^2_{|u,v|}(x_i,y_j)-2\times h_{|u,v|}(x_i,y_j)\times g(x_i,y_j)+g^2(x_i,y_j)\right]$$

The term ($h^2_{\bar{u},\bar{v}}(x_k,y_j)$) is constant and if ($g^2(x_k,y_j)$) is approximately constant then the remaining part is named the Cross-correlation where is extracted as follow: (Lewis, 1995) :

$$C_{\hat{x},\hat{y}}(\bar{u},\bar{v})=\sum_{i=0}^{g\,row}\sum_{j=0}^{g\,column}h_{|u,v|}(x_i,y_j)\cdot g(x_i,y_j) \qquad \text{(A-3)}$$

The final result of this method is a matrix of cross-correlations with the size slightly smaller than the size of search image (exact size is dominated by the size of template). The location of the biggest value of the matrix represents the location of the best match in the second image.

This method causes a large number of summations and multiplications that leads to high computational load. So in many cases, it is demanded to reduce it. One way to overcome this issue is transforming from spatial domain to Fourier (spectral) domain to convert our convolution to a simple multiplication of Fourier transform of both functions, but the author uses a different method to overcome this problem which it explained in methodology.

This formula as a pattern matching core has three disadvantages:

(1) The term ($\sum_{i=0}^{grow}\sum_{j=0}^{gcolumn} g^2(x_k, y_j)$) is assumed as approximately constant but if it varies with the position, matching using this method can fail. For example, it is possible that correlation between a pattern and its exactly match in the second image become smaller than correlation between the pattern and a bright spot.

(2) This method is not invariant to changes in the amplitude of the image. For example, in the case that the changing lighting conditions across the image sequence causes this changes.

(3) The values of Cross-correlation depend on the size of the template.

A way to resolve these disadvantages is inside cross-correlation (convolution) formula, instead, template intensity value in both image, we use its differences from the mean value of the template and divide the output by the standard deviation of both differences, which leads to the following formula:

$$\mathrm{NCC}(u,v)=\frac{\sum_{i=0}^{grow}\sum_{j=0}^{gcolumn}\left[h_{u,v}(x_i,y_j)-\bar{h}_{u,v}\right]\cdot\left[g(x_i,y_j)-\bar{g}\right]}{\sqrt{\sum_{i=0}^{grow}\sum_{i=0}^{gcolumn}\left[h_{u,v}(x_i,y_j)-\bar{h}_{u,v}\right]^2\cdot\sum_{i=0}^{grow}\sum_{j=0}^{gcolumn}\left[g(x_i,y_j)-\bar{g}\right]^2}} \qquad \text{(A-4)}$$

where $\bar{g}$ is mean over template g taken from the first image and $\bar{h}_{u,v}$ is mean of the all value of the template which center of template is located on (u,v) in the second image. The NCC(u,v) is Normalized Cross-Correlation at position (u,v). The final result of this method is a matrix of cross-correlations with the size slightly smaller than the size of search image (exact size is dominated by the size of template). The location of the biggest value of the matrix represents the location of the best match in the second image. Although this formula is not invariant to rotation, it can have good performance even in a noisy image. (Lewis, 1995). Because maximum value of NCCs in the matrix of NCCs dominates the location of best match, in some literature, it called Maximum Cross-Correlation (MCC).

List of figures

List of Tables